universität wien

MASTERARBEIT / MASTER'S THESIS

Titel der Masterarbeit / Title of the Master's Thesis

„Characterisation of ultrathin Ga:YIG films“

verfasst von / submitted by

Aram Sajdak BSc

angestrebter akademischer Grad / in partial fulfilment of the requirements for the degree of

Master of Science (MSc)

Wien, 2023 / Vienna, 2023

Studienkennzahl lt. Studienblatt / degree programme code as it appears on the student record sheet:	UA 066 876
Studienrichtung lt. Studienblatt / degree programme as it appears on the student record sheet:	Masterstudium Physics
Betreut von / Supervisor:	Univ.-Prof. Dr. habil. Andrii Chumak
Mitbetreut von / Co-Supervisor:	Dr. Khrystyna Levchenko

Acknowledgements

First of all, I would like to express my gratitude towards Dr. Khrystyna Levchenko for her continuous support. I was able to experience the process of building up the FMR laboratory to where it is today, as well as getting familiar with the equipment early on in my studies. She also encouraged me to read more into literature and expand my knowledge about the research of the team. Through Prof. Andrii Chumak, I could get the position of a student assistant researcher and work alongside Dr. Levchenko. I am very glad to work with her as a supervisor, but also as a kindhearted colleague. Most of all, I am thankful for her supervision of my Master's Thesis, without which I would certainly not have been able to finish writing. She showed great effort in helping and correcting me, and even answering my questions during the weekend. I also want to earnestly thank Prof. Chumak for the opportunity to work in a research team with many great, young people, excelling in their studies. I am especially thankful for his patience and kind nature, which helped me to overcome the challenges of writing the thesis until now. I would like to thank Rostyslav Serha, who supported me with measurements and provided some illustrations for my thesis. Finally, I also want to thank my parents Artur and In Kyung, my siblings Boram and Garam, as well as my friends Sam, Luke, Benny, Simon, Georg, Marcel, Jan, Emil, Stefan and Jason for their emotional support during the writing, and for the discussions we had.

Abstract

Spin waves attract increasing attention as an alternative information medium in the field of magnonics. Yttrium Iron Garnet (YIG) is one of the most widely known magnonic materials, due to its exceptionally low spin wave damping. The fabrication of high quality single-crystal YIG in the nanoscale has been recently achieved. On this note, it has also been reported that 44 nm thick YIG conduits with a lateral length of 50 nm were fabricated. It was shown that a conduit aspect ratio near unity prevents spin wave scattering into higher width modes. They are thus capable of single mode operation.

For faster, isotropic spin waves, focus of the community has shifted to YIG-substituted materials. Several dopants have been studied, however, their damping is considerably high in the intended spin wave geometries. Gallium doped YIG (Ga:YIG) is a promising magnonic material, due to the higher spin wave group velocity, isotropic spin waves and its intrinsic perpendicular magnetic anisotropy, which makes high bias fields in the forward volume geometry obsolete. Despite that, there are only few experimental studies. The objective of this thesis is to examine ultrathin films of Ga:YIG with a thickness of around 100 nm. This includes the design of an excitation waveguide and determining the anisotropy fields and relaxation parameters via broadband VNA FMR spectroscopy.

In the first chapter I give a brief introduction to magnonics. The current body of research on magnonic materials will be presented, as well as the motivation for the characterisation of Ga:YIG specifically. The second chapter covers the basics of magnetism, including magnetic moment, different magnetic behaviours, interactions between moments, spin wave dynamics, the anisotropy model, and apart from that, FMR in thin films and the kinds of FMR setups. The third chapter revolves around the waveguide design. The necessary theory for microwave engineering will be elucidated: transmission line theory, scattering parameters, skin effect, planar transmission line technologies, discontinuities and transitions, followed by a description of the waveguide design process. The fourth chapter gives an overview of YIG and Ga:YIG. Especially the anisotropy model and the evaluation of the experimental data will be explained there. The fifth chapter lists the results of the waveguide scattering parameter simulation and characterisation, as well as the FMR measurements. The cables characterisation is added. For the FMR data, the evaluation of the anisotropy constants, gyromagnetic ratio, saturation magnetisation, damping parameter and inhomogeneous linewidth broadening is given. The last chapter concludes the results regarding the performance of the designed waveguide and the material parameters of Ga:YIG.

The excitation waveguide was simulated in COMSOL Multiphysics with the Radio Frequency Module. Two designs have been created, and the evaluation led to the conclusion that they would perform very similarly in real experiments. The chosen waveguide was then recreated in Altium Designer to generate the fabrication files. The waveguide was used in the FMR spectroscopy to characterise one reference YIG sample and two Ga:YIG

samples in addition to VSM measurements. The FMR data was analysed in Origin 2019.

In the course of this thesis it has been found that the characterised Ga:YIG samples possess low Gilbert damping and inhomogeneous linewidth broadening ($\alpha_G < 10^{-3}$, $\mu_0 \Delta H(0) \approx 0.4$ mT), a fraction of the initial saturation magnetisation $\mu_0 M_s \approx 20$ mT, and high uniaxial anisotropy $\mu_0 H_{u1} \approx 95$ mT, resulting in perpendicular magnetic anisotropy. These properties make Ga:YIG another milestone in the search for the best magnonic material.

Kurzfassung

Spinwellen erhalten vermehrt Aufmerksamkeit, da sie als Informationsträger in der Magnonik eingesetzt werden können. Yttrium Eisen Granat (YIG) ist eines der bekanntesten magnonischen Materialen wegen seiner sehr niedrigen Spinwellendämpfung. Die Herstellung von hochwertigen Einkristallen von YIG im Nanobereich wurde vor Kurzem berichtet. In Verbindung damit wurden 44 nm dicke, 50 nm lange YIG Leitungen untersucht, die ein Seitenverhältnis nahe von 1 haben. Diese ermöglichen einen Betrieb in einem einzigen Spinwellenmodus und verhindern die Streuung und Kopplung des Signals.

Für schnellere, isotrope Spinwellen richtet sich der Fokus der Wissenschaftler auf YIG-substituierte Materiale. Einige Dotiermittel wurden bereits untersucht, aber die Messungen haben ergeben, dass die Dämpfung in den gewünschten Spinwellengeometrien relativ hoch ist. Gallium dotiertes YIG (Ga:YIG) ist ein attraktiver magnonischer Stoff wegen seiner höheren Spinwellengeschwindigkeit, der isotropen Spinwellen, und seiner intrinsischen senkrechten Magnetisierung, die den Betrieb in Forward Volume Geometrie begünstigen. Bisher gibt es nur wenige experimentelle Untersuchungen. Daher ist das Ziel dieser Arbeit, ultradünne Filme von Ga:YIG mit einer Stärke von ungefähr 100 nm zu charakterisieren. Dafür wird ein Wellenleiter designt, und die Anisotropie Beiträge, sowie die Relaxationsparameter mittels Breitband VNA FMR Spektroskopie ermittelt.

Im ersten Kapitel gebe ich eine kurze Einleitung in die Magnonik. Die Forschung zu magnonischen Materialen und die Motivation zur Charakterisierung von Ga:YIG werden besprochen. Das zweite Kapitel deckt die Grundlagen von Magnetismus ab, wie das magnetische Moment, verschiedene Magnettypen, Wechselwirkungen zwischen Momenten, Spinwellendynamik, das Anisotropiemodell, und zusätzlich FMR in dünnen Filmen, sowie die Arten von FMR Setups. Das dritte Kapitel handelt von dem Wellenleiter Design. Die notwendige Theorie über Mikrowellentechnik wird erklärt: Transmissionslinien, Streuung, Skin Effekt, Unterbrechungen und Übergänge, gefolgt von der Beschreibung des Wellenleiter Design Prozesses. Das vierte Kapitel gibt einen Überblick über YIG und Ga:YIG. Vor allem das Anisotropiemodell und die Evaluierung der experimentellen Daten wird hier beschrieben. Das fünfte Kapitel zeigt die Ergebnisse der Wellenleiter Simulationen und Charakterisierung, sowie die FMR Messungen. Dabei werden zwei Wellenleiter Designs, der hergestellte Wellenleiter und ein kommerzieller Wellenleiter untersucht. Die FMR Daten geben Aufschluss über die Anisotropie Konstanten, das gyromagnetische Verhältnis, die Sättigungsmagnetisierung, den Dämpfungsparameter und die inhomogene Ausbreitung der Linienbreite. Das letzte Kapitel fasst die Ergebnisse der Wellenleiter Performance und der Materialparameter von Ga:YIG zusammen.

Der Wellenleiter wurde in COMSOL Multiphysics mit dem Radio Frequency Modul simuliert. Zwei Designs wurden erstellt, und deren Vergleich hat ergeben, dass sie ähnlich gut in echten Experimenten laufen würden. Der gewählte Wellenleiter wurde dann in Altium

Designer nachgebildet, um die Dateien zur Herstellung zu generieren. Der Wellenleiter wurde in der FMR Spektroskopie verwendet, um eine Referenzprobe YIG und zwei Proben Ga:YIG zu charakterisieren, zusätzlich zu VSM Messungen. Die Ergebnisse wurden in Origin 2019 analysiert.

Im Rahmen dieser Arbeit hat sich ergeben, dass die Ga:YIG Proben eine geringe Gilbert Dämpfung und inhomogene Ausbreitung der Linienbreite ($\alpha_G < 10^{-3}$, $\mu_0 \Delta H(0) \approx 0.4$ mT), einen Bruchteil der ursprünglichen Sättigungsmagnetisierung $\mu_0 M_s \approx 20$ mT, sowie eine hohe uniaxiale Anisotropie $\mu_0 H_{u1} \approx 95$ mT aufweisen. Letzteres führt zu einer bevorzugten Magnetisierung senkrecht zum Film. Diese Eigenschaften machen Ga:YIG zu einem weiteren Meilenstein in der Suche nach dem besten magnonischen Material.

Contents

List of Tables

List of Figures

1 Introduction

Spin waves are a collective motion of the electron spin subsystem in a magnetically ordered material. [10] The wave characteristics depend on several factors like the choice of magnetic material, the shape of the sample, and the magnetic bias field. [11] [12] The presence of linear and nonlinear spin-wave properties makes them an interesting subject for further studies. Several investigations have already been conducted, with reports about one- and two-dimensional soliton formation [13] [14], wavefront reversal processes [15] [16], and room temperature Bose-Einstein condensation of magnons [17] [18], among others.

Recently, spin waves attracted more attention because they can be used as alternative information carriers. The field of magnonics [19] revolves around magnons – quanta of spin waves – and their implementation in magnonic circuits. Magnonics comes with some advantages over commercial computing, such as higher clock rates, no Joule heat dissipation, nanofabrication, and wave-based computing. [20]

Yttrium Iron Garnet (YIG) [9] lends itself to the pool of available materials, partly due to its exceptionally low spin wave damping. Recently, a study reported the successful fabrication of sub-10 nm thick YIG conduits. [21] However, the fastest observed dipolar waves are anisotropic magnetostatic surface waves, with a group velocity of approximately 0.2 µm/ns. [22] To address this issue, several YIG-substituted materials [23] [24] [25] [26] [27] have been researched to find an alternative that allows fast, isotropic spin waves.

Gallium doped YIG (Ga:YIG) [2] [28] [29] is a promising prospect, in that it offers a higher group velocity at lower saturation magnetisation, isotropic spin waves due to an exchange dominated dispersion relation, and perpendicular magnetic anisotropy, which lowers the required bias field. In this thesis, I will characterise two thin film Ga:YIG samples via ferromagnetic resonance (FMR) spectroscopy and compare them with a reference YIG sample. In addition, I will design a waveguide that aims to increase the maximum measurement range of FMR spectroscopy.

2 Theoretical basics

This chapter introduces the necessary terms and definitions to provide the reader with a basis of knowledge in magnetism and interactions of magnetic nature. (cf. [30]) Magnetism can be described by two distinct unit systems, **SI** and **CGS**. They can be converted into one another. Hence, the formulas given in SI units will be different than in CGS. Throughout this thesis I will adhere to the SI unit system, and only when specifying the CGS formalism will I write units in CGS.

There are two fundamental sources that give rise to magnetism: electric current, and magnetic moments of elementary particles $\mathbf{m}$. The magnetic field $\mathbf{H}$, the magnetisation $\mathbf{M}$ and the permeability of free space μ_0 form the magnetic flux or induction $\mathbf{B}$:

$$\mathbf{B} = \mu_0(\mathbf{H} + \mathbf{M}) \tag{2.1}$$

where $\mathbf{M} = \sum^i \mathbf{m}_i/V$ is the sum of magnetic moments normalised per unit volume, and $\mu_0 = 4\pi \cdot 10^{-7} NA^{-2}$. $\mathbf{B}$ is characterised as the material response to a magnetic field. Other key expressions are the susceptibility $\chi = M/H$ and the permeability $\mu = B/H$.

Since in the field of magnonics electric current is used in addition to or replaced by spin-wave dynamics [19], I put my focus on magnetic moments, which govern the properties and performance of magnonic materials.

2.1 Magnetic moments

If a solid is located in a uniform magnetic field, the object's internal and induced magnetic moments interact with the field. The magnetic moments $\mathbf{m}$ experience a torque τ, which forces them to align with the field $\mathbf{H}$. It holds [31]:

$$\tau = \mathbf{m} \times \mathbf{B} \tag{2.2}$$

The force acting on the moments is calculated as follows:

$$F = \nabla (\mathbf{m} \cdot \mathbf{B}) \tag{2.3}$$

whereas the potential energy is given by:

$$E_{pot} = -\mathbf{m} \cdot \mathbf{B} \tag{2.4}$$

2.1.1 Calculation of magnetic moments

To calculate the magnetic moment of an atom, first consider the Bohr model of the atom. (cf. [32]) The electron orbits the nucleus in a circular loop with radius r and spins around

its own axis. The orbital motion of the electron is equivalent to a current I running through a wire loop with an area vector $\mathbf{A} = A\mathbf{n} = \pi r^2\mathbf{n}$, where $\mathbf{n}$ is the unit normal vector of the area. This induces a magnetic moment:

$$\boldsymbol{\mu}_l = I \cdot A \tag{2.5}$$

The charge of the electron -e is known. The angular velocity of the electron ω then determines the current I:

$$I = -\frac{e\omega}{2\pi} \tag{2.6}$$

Combining the expressions for I and A, we get:

$$\boldsymbol{\mu}_l = -\frac{e\omega r^2}{2}\mathbf{n} \tag{2.7}$$

The result can be expressed in terms of the angular momentum $\mathbf{L}$ for an electron:

$$\mathbf{L} = m_e\omega r^2\mathbf{n} \tag{2.8}$$

$$\boldsymbol{\mu}_l = -\frac{e}{2m_e}\mathbf{L} \tag{2.9}$$

where m_e is the mass of an electron.

Since in the Bohr atom model, we assume the orbital angular momentum to be a multiple of $\hbar$, we can set:

$$\boldsymbol{\mu}_l = -\frac{g_l\mu_B}{\hbar}\mathbf{L} \tag{2.10}$$

$$\mu_B = \frac{e\hbar}{2m_e} \tag{2.11}$$

Here the Bohr magneton μ_B is introduced. In addition, the Landé g factor g_l is also included, where $g_l = 1$ for orbital angular momentum. For electrons with the orbital quantum number $0 \leq l \leq n - 1$ and main quantum number n, it holds:

$$|\mathbf{L}|^2 = l(l+1)\hbar^2 \tag{2.12}$$

The electron also has a spin, with its corresponding spin quantum number s = 1/2. For all practical purposes, it behaves like angular momentum, and similar to the orbital angular momentum, the spin generates a magnetic moment:

$$\boldsymbol{\mu}_s = -\frac{g_s\mu_B}{\hbar}\mathbf{s} \tag{2.13}$$

where g_s is the Landé g factor for electron spin, and takes the value of approximately $g_s \approx 2$. ($g_s/2 = 1.00115965218085(76)$ [33]) Analogously to $|\mathbf{L}|^2$ we can compute $|\mathbf{s}|^2 = s(s+1)\hbar^2$.

The orbital angular momentum and spin angular momentum can be summarised in a total angular momentum $\mathbf{J}$, where I introduce the gyromagnetic ratio γ, which negates the need for two different Landé g factors:

$$\boldsymbol{\mu}_m = \frac{g_j \mu_j}{\hbar} \mathbf{J} = \gamma \mathbf{J} \tag{2.14}$$

μ_j is defined as the magneton of a particle with the total angular momentum $\mathbf{J}$, the charge q, and the mass m_j:

$$\mu_j = \frac{q\hbar}{2m_j} \tag{2.15}$$

If an external magnetic field is applied in z direction, the magnetic dipoles align themselves to it. The projection of the magnetic moment onto the z axis is then given by:

$$|\boldsymbol{\mu}_{m,z}| = \frac{g_j \mu_j |J_z|}{\hbar} \tag{2.16}$$

2.2 Interactions between magnetic moments

The permanent magnetic moments in a solid can couple with each other and establish magnetic order within the object. The cause of this is two main interactions: the classical dipolar interaction and the exchange interaction rooted in quantum mechanics. First, the interactions between magnetic moments will be covered, followed by an overview of the types of magnetism in materials.

2.2.1 Dipolar interaction

The dipolar interaction energy E_{dip} of two magnetic moments $\boldsymbol{\mu}_i$ and $\boldsymbol{\mu}_j$ at the positions $\mathbf{r}_i$ and $\mathbf{r}_j$, respectively, and $\mathbf{r}_{ij} = \mathbf{r}_i - \mathbf{r}_j$, is given by [34]:

$$E_{dip} = \frac{\mu_0}{4\pi} \left[\frac{\boldsymbol{\mu}_i \cdot \boldsymbol{\mu}_j}{\mathbf{r}_{ij}^3} - 3 \frac{(\boldsymbol{\mu}_i \cdot \mathbf{r}_{ij})(\boldsymbol{\mu}_j \cdot \mathbf{r}_{ij})}{\mathbf{r}_{ij}^5} \right] = -\mu_0 \boldsymbol{\mu}_i \cdot \mathbf{H}_{dip} \tag{2.17}$$

$\mu_0 \mathbf{H}_{dip}$ is the dipole field generated by μ_j. Considering a many-particle system, the definition of E_{dip} slightly changes:

$$E_{dip} = -\langle \mu_0 \boldsymbol{\mu}_i \cdot \mathbf{H}_{dip} \rangle \tag{2.18}$$

Here, $\mu_0 \mathbf{H}_{dip}$ is generated by all the other dipoles in the system.

However, the resulting energy of the dipole interaction is equivalent to the thermal energy at around $T \approx 0{,}1$ K. Therefore, it is not sufficient to maintain a magnetic lattice at room temperature. The dipolar interaction becomes more important at greater distances, though. One example is the resulting demagnetising field, which influences the spin dynamics.

2.2.2 Exchange interaction

In contrast to the dipolar interaction, the exchange interaction is isotropic and strongly depends on the distance between neighbour spins. (cf. [3]) The Weiss theory of ferromagnetism [35] postulates an internal field inside of the bulk magnet. It is responsible for forming the domains of uniform magnetisation. Unfortunately, it is not possible to explain

this Weiss "molecular" field classically, and a quantum physical explanation is underway.

A simple model is the two-electron system of two hydrogen atoms, A and B. The electrons form a covalent bond and are described by the wave functions $\Psi_A(r_1)$ and $\Psi_B(r_2)$. The probabilities of finding them at positions r_1 and r_2 are calculated with $|\Psi_A(r_1)|^2$ and $|\Psi_B(r_2)|^2$, respectively. When the hydrogen atoms approach each other, the electrons can either be in a bonding state or in an antibonding state, where they are localised between the nuclei or away from the nuclei, respectively. In the case of the bonding state, there exists a perfect internuclear distance R_0, at which the energy of the system is minimised. An energy level diagram for the system is also given in fig. 2.1.

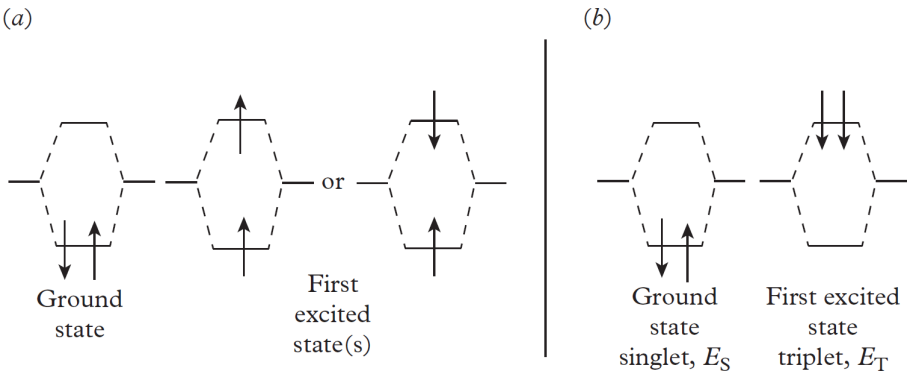

Figure 2.1: Energy level diagram for a) two one-electron systems and b) a two-electron system. Taken from [3].

Assuming we isolate the electrons and only look at a one-electron model, there exists a ground state and two first excited states. There are two choices for the first excited state because the other electron could either be parallel or antiparallel to the first one. Comparing this to the two-electron system, we get the same ground state as before, but only one first excited state. These states are called the singlet state and the triplet state, with energy levels E_S and E_T, respectively. The Pauli exclusion principle dictates that either the wave functions are asymmetrical and the spins parallel, or the wave functions are symmetrical and the spins are antiparallel, resulting in the two states.

Now, with the specific energy levels, the exchange energy J is defined as:

$$-J = E_T - E_S \tag{2.19}$$

If $J > 0$, then the system prefers a parallel alignment of the electron spins, This implies ferromagnetic behaviour.

It was shown that the orbital wave functions and the constraints from the Pauli exclusion principle lead to the exchange interaction. Even though we have not considered the magnetic moment of the electrons, a spin-spin coupling is still evident. Dirac showed that this exchange coupling energy is determined by

$$E_{ij}^{exch} = -2J_{ij}\mathbf{S}_i \cdot \mathbf{S}_j \tag{2.20}$$

where J_{ij} is the exchange integral between the atoms i and j, and $\mathbf{S}_i$, $\mathbf{S}_i$ are the spin angular momenta given in units of $\hbar$. J_{ij} is short-ranged and usually just includes nearest neighbour interactions, in some cases also next nearest neighbour interactions. The magnitude of these fields is unbounded by the equations, and as such, the internal fields can become very large.

It has to be mentioned that anisotropy has been observed in ferromagnetic materials, even though the exchange interaction is shown to be isotropic. The reason lies within the orbital angular momentum. For the sake of simplicity, I set $L = 0$, but in most cases it cannot be ignored. In crystalline materials, the crystal structure results in an orbital alignment along specific crystallographic directions. The spins couple to the orbitals and this *spin-orbit coupling* becomes the reason for magnetocrystalline anisotropies.

2.2.3 Types of magnetism in materials

Diamagnetism

Atoms and compounds with a vanishing effective magnetisation, materials with full electron shells like noble gases, ionic solids, or semiconductors with strong covalent bonding exhibit what is called diamagnetic behaviour. In these materials, the electrical charges serve to partially shield the material from magnetic fields. Diamagnets therefore have a small negative susceptibility. The reason for this is that the electron orbits precess around the bias field, such that the induced magnetisation opposes the field. Ideal superconducting materials are special diamagnets with χ = -1. In other words, in their superconducting state, they expel all magnetic flux.
As a side note, all atoms and molecules exhibit diamagnetism, but it is subtle by nature, and in all other materials the diamagnetic behaviour is dominated by the response of atomic magnetic moments to an applied field by a large margin.

Paramagnetism

Paramagnetic materials consist of an ensemble of individual atoms, each with a magnetic moment $\mathbf{m}$, however, the interaction between them is negligible. At room temperature, the thermal energy of the environment is high enough to randomise the orientation of the magnetic moments (for the formula, see **Dipolar interaction**). Therefore, without a bias field, the net magnetisation $\mathbf{M} = 0$. In the presence of a field, some magnetic moments get rotated towards the field direction, which then results in a nonzero net magnetisation and positive susceptibility. The magnetisation $\mathbf{M}$ increases linearly with the applied field. Now consider the temperature. At a constant bias field, the increase in temperature leads to a decrease in net magnetisation. The thermal energy thus counteracts the alignment of the magnetic moments. This inverse proportional relation is known as the Curie law of paramagnetism.

Ferromagnetism

Ferromagnetism builds upon individual atoms with a net magnetic moment but in addition the neighbouring atoms couple with each other via the exchange interaction. The magnetic moments or spins of the neighbour atoms align themselves parallel to each other, either ↑↑

or $\rightarrow\rightarrow$. The magnetic moments also get spontaneously magnetised and split into domains of uniform magnetisation. In the absence of an external field the domains' orientations result in a net magnetisation of 0, to minimise the magnetostatic energy.
Now, in ferromagnetic materials the response to external magnetic fields is nonlinear. They exhibit hysteresis, from which material characteristics and magnetisation history can be deduced. Reverting the field would not lead to the same magnetisation as was in the beginning. This hysteresis is characteristic in ferro- and ferrimagnetic materials (for ferrimagnets, see **Ferrimagnetism**). Given a strong enough external field, then all the magnetic moments are aligned and the object is fully magnetised along this direction. This value of magnetisation is the *saturation magnetisation* M_s.
With increasing temperature, the hysteresis remains, but the saturation magnetisation decreases. This holds until the thermal energy is strong enough to overcome the exchange interaction between the neighbour atoms. At this point, the saturation magnetisation reaches 0. This temperature is called the Curie temperature T_C. At $T > T_C$ the object acts as a paramagnet, and it satisfies the Curie-Weiss law of ferromagnetism:

$$\chi = \frac{C}{T - T_C} \tag{2.21}$$

Note that this equation yields a divergence at the Curie temperature T_C. This is true for the intrinsic susceptibility of the material $\chi_{mat} = M/H_{in}$, with the magnetic field $\mathbf{H}_{in} = \mathbf{H}_{app} - N_d\mathbf{M}$ inside of the material (N_d is the *demagnetising factor*, which will be covered in the section **Demagnetising field**). However, the experimentally measured susceptibility $\chi_{sample} = M/H_{app}$ is sample dependent. The two susceptibilities are related to each other as follows:

$$\chi_{sample} = \frac{\chi_{mat}}{1 + N_d\chi_{mat}} \tag{2.22}$$

Hence, as the temperature goes to T_C, the susceptibility χ_{sample} only reaches a maximum of $1/N_d$.

Antiferromagnetism

Contrary to ferromagnetism, the exchange coupling in antiferromagnets favours the antiparallel alignment between magnetic moments of neighbour atoms. The magnet consists of two identical interpenetrating, antiparallel lattices inside the magnet. In case those lattices are perfectly aligned there exists no net magnetisation nor spontaneous magnetisation. Many antiferromagnets are known to exhibit paramagnetic behaviour at room temperature but below the so-called Néel temperature T_N the susceptibility changes. Additionally, below T_N the susceptibility becomes dependent on the direction of the external field. The field $\mathbf{H}$ is split into the two components $\mathbf{H}_\parallel$ and $\mathbf{H}_\perp$, parallel and perpendicular to the preferential direction of the spin-lattice, respectively. For $T > T_N$ the susceptibility of an antiferromagnet is given:

$$\chi = \frac{C}{T - \theta} = \frac{C}{T + T_N} \tag{2.23}$$

where θ = -T_N is the intercept of $1/\chi$, when it is extrapolated from $T > T_N$ to $T < 0$.

Ferrimagnetism

Ferrimagnets also have antiparallel sublattices. Just like with antiferromagnets, the exchange interaction favours the antiparallel alignment. However, the sublattice moments do not compensate each other in general. The sublattices are either occupied by two different types of ions with unequal magnetic moments oriented in opposite directions or by one kind of ion with different concentrations in the sublattices. Therefore, below T_C the magnet shows spontaneous magnetisation. This implies that ferrimagnets share common properties with ferromagnets. Under T_C they exhibit spontaneous magnetisation, domains, saturation magnetisation, hysteresis, and above T_C they behave like paramagnets. Ferrimagnetism is usually observed in oxides. YIG and Ga:YIG are also part of this group.

2.2.4 Effective magnetic field

If a solid is located inside of a magnetic field, then the field in the solid does not necessarily equal the external field $\mu_0\mathbf{H}_{ext}$. There are several fields generated that affect the internal field, which in turn creates the effective field:

$$\mu_0\mathbf{H}_{eff} = \mu_0\mathbf{H}_{ext} + \mu_0\mathbf{h}(t) + \mu_0\mathbf{H}_{ex} + \mu_0\mathbf{H}_{demag} + \mu_0\mathbf{H}_{ani} + \dots \tag{2.24}$$

The additional terms are the time-dependent component of the external field $\mu_0\mathbf{h}(t)$, the previously introduced exchange field $\mu_0\mathbf{H}_{ext}$ and the anisotropy field $\mu_0\mathbf{H}_{ani}$. Since the anisotropy in Ga:YIG is one of the key points in the research question, the theory and calculation in the experimental setup will be discussed in separate chapters. The demagnetising field $\mu_0\mathbf{H}_{demag}$ is new as well. (see **Demagnetising field**) We can summarise all terms on the right-hand side of the equation:

$$\mathbf{H}_{eff} = -\frac{1}{\mu_0}\nabla_{\mathbf{M}}(\epsilon) \tag{2.25}$$

The effective field is therefore proportional to the gradient of the energy density ϵ with respect to the magnetisation $\mathbf{M}$. In other words, it is equivalent to the change in the energy density at the displacement of the magnetisation.

2.2.5 Demagnetising field

The demagnetising field can be described with the dipolar interaction introduced earlier. (cf. [36], [37]) Let us look at an infinitely large, homogeneous solid, then the dipole fields generated by the magnetic moments cancel each other out. However, this is not the case in a finite volume, in thin films, or inhomogeneous solids. Hence, the finite magnetic structure at the boundaries and domain walls gives rise to stray fields, which oppose the internal magnetisation. These are called the demagnetising field $\mu_0 H_{demag}$.

Consider a magnetised body. The magnetisation can be thought of as magnetic monopoles on the body surface. Then the density of *surface poles* σ is given by

$$\sigma = \mathbf{M} \cdot \mathbf{n} \tag{2.26}$$

where $\mathbf{n}$ is the unit normal vector at any given point on the surface of the body. In this model, the surface poles generate a force field, which runs through the whole body. The

demagnetising field changes according to the shape (*shape anisotropy*) and the size of the sample. In order to fully magnetise samples to saturation magnetisation, work has to be done to counteract this field. If H_{demag} is uniform, then we can calculate the demagnetising energy:

$$E_{demag}/volume = \mu_0 \int_0^M \mathbf{H}_{demag} \cdot d\mathbf{M} \tag{2.27}$$

A minimum of E_{demag} is achieved by the formation of domains.

The magnetic flux in this example is as follows

$$\mathbf{B} = \mu_0(\mathbf{H}_{ext} + \mathbf{M} + \mathbf{H}_{demag}) \tag{2.28}$$

Assume that $\mathbf{H}_{demag}$ = -$N_d\mathbf{M}$. In other words, the demagnetising field is proportional to the magnetisation. After changing the expression, we get

$$\mathbf{B} = \mu_0(\mathbf{H}_{ext} + \mathbf{M}(1 - N_d)) \tag{2.29}$$

2.2.6 Calculating the demagnetising factor for various geometries

Sphere

Let us start with the example of a sphere with radius *a*. It is magnetised along the vertical direction. Thus, the surface pole density gradually approaches 0 as we get closer to the equatorial plane. The infinitesimal area element on the sphere surface is given as dA = $2\pi a \sin\theta a d\theta$. The poles create a field inside the sphere. The field component in the centre can then be found via the inverse square law relationship:

$$H = \frac{p}{4\pi a^2} \tag{2.30}$$

$$dH_{d\perp} = -2\pi a \sin\theta a d\theta M \cos\theta^2 / 4\pi a^2 = -(M/2)\sin\theta\cos\theta^2 d\theta \tag{2.31}$$

The negative sign denotes that the field is antiparallel to **M**. Due to symmetry considerations, it is sufficient to calculate $H_{d\perp}$ for N_d. Since the contribution from both halves is the same, it is convenient to integrate only over one half of the sphere and multiply by 2:

$$H_d = -2\int_0^{\pi/2} (M/2)\sin\theta\cos\theta^2 d\theta = -M/3 \tag{2.32}$$

So it yields $N_d = 1/3$. In addition, the isotropy and spherical symmetry allow us to infer the demagnetising factor for any arbitrary magnetisation direction. So, if *a, b, c* are the principal directions in a Cartesian coordinate system, then N_d will remain the same along all axes:

$$N_a = N_b = N_c = 1/3 \tag{2.33}$$

In fact, the following relationship is true for all ellipsoids of revolution:

$$N_a + N_b + N_c = 1 \tag{2.34}$$

Oblate spheroid ($b = c \neq a,\ c/a = r$)

The a direction is the axis of revolution here. For N_a we get

$$N_a = \frac{r^2}{r^2-1}\left[1 - \sqrt{\frac{1}{r^2-1}}\sin^{-1}\sqrt{\frac{r^2-1}{r}}\right] \tag{2.35}$$

Finding the limit for $r \to \infty$, the result is $N_a = 1,\ N_b = N_c = 0$. The oblate spheroid can be used as a model for flat thin films.

2.3 Dynamics of the magnetic order

The previous chapter provided a thorough overview of magnetostatics. This chapter of the thesis is dedicated to the dynamics of magnetism. I will derive the equation of motion for a magnetic moment and deduce from it the dynamics of the magnetisation vector. (cf. [38]) Solutions to the equation are the various spin waves, as well as modes of magnetisation oscillation, on which I will focus in the chapter **Ferromagnetic resonance**.

2.3.1 Landau-Lifshitz-Gilbert equation

Consider a magnetised ferromagnet placed in an external magnetic field $\mathbf{H}_0$. The effective field inside of the magnet $\mathbf{H}_{eff}$ will then induce a precessional motion of the magnetic moments. (see fig. 2.2) The displacement out of the initial state is connected to the torque the magnetic moments experience:

$$\tau = \frac{d\mathbf{J}}{dt} = \boldsymbol{\mu}_m \times \mathbf{B}_{eff} \tag{2.36}$$

The atomic magnetic moment can be expressed in terms of the total angular momentum $\mathbf{J}$:

$$\boldsymbol{\mu}_m = -\frac{g\mu_B}{\hbar}\mathbf{J} = -\gamma\mathbf{J} \tag{2.37}$$

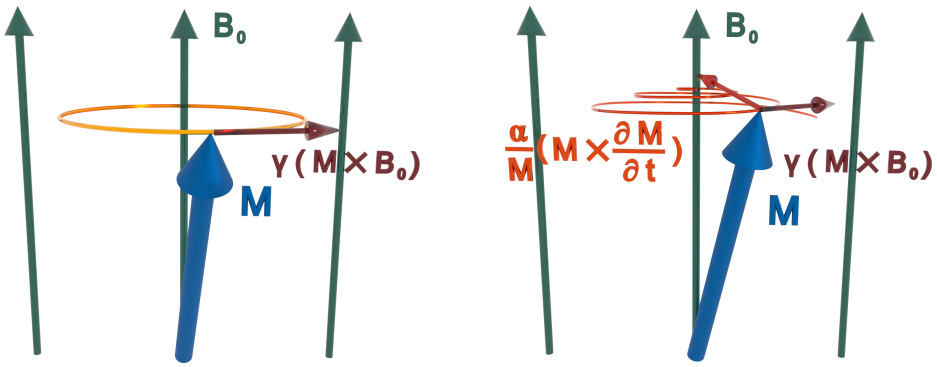

Figure 2.2: The precessional motion of $\mathbf{M}$ around $\mathbf{B}_{eff} \equiv \mathbf{B}_0$ (isotropic medium): (l.) without damping (r.) with damping. Author: Rostyslav Serha. Reprinted with the permission of the author.

where $\hbar$ is the reduced Planck constant and $\gamma = \frac{g\mu_B}{\hbar}$ is the gyromagnetic ratio of the free electron. Plugging (2.37) into (2.36) gives

$$\tau = -\frac{1}{\gamma}\frac{d\boldsymbol{\mu}_m}{dt} = \boldsymbol{\mu}_m \times \mathbf{B}_{eff} \tag{2.38}$$

Multiplying (2.38) with the number of magnetic moments in a unit volume N and γ, we arrive at the Landau-Lifshitz torque equation with the magnetisation $\mathbf{M}$:

$$\frac{d\mathbf{M}}{dt} = -\gamma \mathbf{M} \times \mathbf{B}_{eff} \tag{2.39}$$

This equation describes the precession of the magnetisation around an effective field. However, it is only valid for uniform magnetisation, and approximately if $\mathbf{M}$ varies slowly in space. It also does not allow for losses, i.e. the dissipation of energy during the precession motion. Gilbert added a phenomenological damping term to include the dissipation:

$$\frac{d\mathbf{M}}{dt} = -\gamma \mathbf{M} \times \mathbf{B}_{eff} + \frac{\alpha_G}{M_s}\left(\mathbf{M} \times \frac{d\mathbf{M}}{dt}\right) \tag{2.40}$$

The Gilbert damping parameter is denoted as α_G. It is strictly positive: $\alpha_G > 0$, and the magnitude of damping is given by the time dependence of the magnetisation. The equation (2.40) is also called the Landau-Lifshitz-Gilbert equation. (LLG)

2.3.2 Excitation of magnetisation precession

In this thesis, the dynamic magnetic fields are thought to be the origin of the magnetisation. Therefore the description of the magnetic system builds upon time-dependent magnetic fields. First of all, the effective field and magnetisation are both split into a dynamic part and a static part [39]:

$$\mathbf{H}_{eff}(t) = \mathbf{H}_0 + \mathbf{h}(t) \tag{2.41}$$

$$\mathbf{M}(t) = \mathbf{M}_0 + \mathbf{m}(t) \tag{2.42}$$

Plugging this into the Landau-Lifshitz equation results in:

$$\frac{d\mathbf{M}_0}{dt} + \frac{d\mathbf{m}(t)}{dt} = -\gamma\mu_0[\mathbf{M}_0 \times \mathbf{H}_0 + \mathbf{M}_0 \times \mathbf{h}(t) + \mathbf{m}(t) \times \mathbf{H}_0 + \mathbf{m}(t) \times \mathbf{h}(t)] \tag{2.43}$$

$\frac{d\mathbf{M}_0}{dt} = 0$ as per definition, since this is the static part of magnetisation. Further, assume that the static magnetic field is parallel to the static magnetisation and that the solid is homogeneously magnetised. Then it holds $\mathbf{M}_0 \parallel \mathbf{H}_0$, and further $\mathbf{M}_0 \times \mathbf{H}_0 = 0$. In addition, we can assume that the dynamic parts are small compared to the static parts: $|\mathbf{M}_0| \gg |\mathbf{m}(t)|$, $|\mathbf{H}_0| \gg |\mathbf{h}(t)|$. Then, in the first approximation, the last term in (2.43) can be omitted.

Using the ansatz

$$\mathbf{m}(t) = \mathbf{m}_0 \exp(-i\omega t) \tag{2.44}$$

$$\mathbf{h}(t) = \mathbf{h}_0 \exp(-i\omega t) \tag{2.45}$$

with the approximations in (2.43), the linearised Landau-Lifshitz equation will be obtained:

$$i\omega\mathbf{m} + \gamma\mu_0\mathbf{m} \times \mathbf{H}_0 = -\gamma\mu_0\mathbf{M}_0 \times \mathbf{h} \tag{2.46}$$

The projection onto a Cartesian coordinate system ($\vec{z} \parallel \mathbf{M}_0 \parallel \mathbf{H}_0$) leads to a system of equations:

$$\begin{aligned} i\omega m_x + \gamma\mu_0 m_y H_0 &= \gamma\mu_0 M_0 h_y \\ i\omega m_y - \gamma\mu_0 m_x H_0 &= \gamma\mu_0 M_0 h_x \\ i\omega m_z &= 0 \end{aligned} \tag{2.47}$$

The solution to (2.47) now sets the dynamic parts of the magnetisation and the magnetic field in relation to each other:

$$\mathbf{m}(t) = \tilde{\chi}\mathbf{h}(t) \tag{2.48}$$

Here I introduce the Polder susceptibility tensor $\tilde{\chi}$:

$$\tilde{\chi} = \begin{pmatrix} \chi & i\chi_a & 0 \\ -i\chi_a & \chi & 0 \\ 0 & 0 & 0 \end{pmatrix} \tag{2.49}$$

where

$$\chi = \frac{\omega_\mathrm{M}\omega_\mathrm{H}}{\omega_\mathrm{H}^2 - \omega^2}, \quad \chi_a = \frac{\omega_\mathrm{M}\omega}{\omega_\mathrm{H}^2 - \omega^2} \tag{2.50}$$

$$\omega_\mathrm{H} = \gamma\mu_0 H_0, \quad \omega_\mathrm{M} = \gamma\mu_0 M_0 \tag{2.51}$$

Hence, the response to an external excitation is determined by $\tilde{\chi}$. This is the description of the magnetisation dynamics. Furthermore, if the excitation occurs at the frequency ω_H, then this leads to a singularity in the components of the susceptibility tensor, which corresponds to the nonexistent magnetic damping in the Landau-Lifshitz equation. Those singularities can be avoided by reintroducing the damping in the substitution $\omega_\mathrm{H} \longrightarrow \omega_\mathrm{H} + i\alpha\omega$.

2.4 Magnetocrystalline anisotropy

In a magnetically anisotropic material, the magnetic state exhibits a dependence on the direction of the magnetisation. More specifically, in a magnetic solid, there exists an orientation of the magnetisation, for which the energy of the system is minimised. Spin-orbit coupling and the dipolar interaction set the preferred magnetisation axes in the crystal lattice or the geometry of the magnet, respectively. If the applied external field is misaligned with the preferential direction of magnetisation, then the field exerts work on the system in order to displace the magnetisation. I shall shortly discuss the magnetocrystalline anisotropy (MCA).

2.4.1 Computation of the magnetocrystalline anisotropy

The MCA is caused by the spin-orbit interaction in the underlying crystal structure of the magnetic solid. Szymczak and Tsuya [40] have obtained the expression for the energy of the MCA in thin films of cubic crystal lattices, and it is accurate up to the fourth order in the directional cosines of magnetisation:

$$U_{\mathrm{A}} = A\alpha_1^2\beta_1^2 + B\alpha_1\alpha_2\beta_1\beta_2 + C\beta_1^4(3\alpha_1^2 - 1) + D\beta_1^2\beta_2^2(3\alpha_3^2 - 1)$$
$$+E\beta_1^2\beta_2\beta_3\alpha_2\alpha_3 + F\beta_1^2\alpha_1^4 + G\alpha_1^2\alpha_3^2\beta_2^2 + H\alpha_1^2\alpha_2\alpha_3\beta_2\beta_3 + \text{c.p.} \tag{2.52}$$

where A, B, ..., H are anisotropy constants, β_i are the directional cosines of the crystallographic axes, α_i are the directional cosines of magnetisation and c.p. stands for cyclic permutations. If another term contributes to the MCA, it is possible to split the energy term into two parts [1]:

$$U_A = U_A^{\text{cubic}} + U_A^{\text{non cubic}}$$

The noncubic term comes from the presence of other anisotropies.
As an example: YIG is a cubic crystal. However, the lattice mismatch between YIG and its substrate leads to a compressive strain in the film plane, resulting in uniaxial anisotropy.

In the presence of magnetic anisotropy, the magnetic permeability μ is no longer a single value and becomes a tensor with the general form:

$$\hat{\mu} = \begin{pmatrix} \mu_{11} & \mu_{12} & 0 \\ \mu_{21} & \mu_{22} & 0 \\ 0 & 0 & 1 \end{pmatrix} \tag{2.53}$$

2.5 Ferromagnetic resonance

The previous chapters help examine the phenomenon of magnetic resonance. In the section **Excitation of magnetisation** the reader became familiar with the idea of using a small dynamic magnetic field $\mathbf{h}(t)$. It serves to excite spin waves and/or magnetisation oscillations in the sample. If excitation occurs close to the resonance frequency ω_{res}, then the excitation is at its maximum.

The uniform in-phase precession of spins in a ferro-, ferri-, or antiferromagnetic material is called *ferromagnetic resonance* (FMR). [41][11][12][42] FMR is no wave propagation mode, therefore k = 0.

2.5.1 Ferromagnetic resonance in a thin film

Suppose we want to excite FMR. The resonance frequency ω_{res} depends on the effective magnetic field $\mu_0\mathbf{H}_{eff}$. It was already mentioned that one contribution to it is the demagnetising field $\mu_0\mathbf{H}_{demag}$, which depends primarily on the shape of the sample. Using the demagnetising factors N_d from **Demagnetising field** and the Kittel equations we can calculate ω_{res} for an isotropic ferromagnet.

As an example, let us look at the oblate spheroid with $N_a = 1,\ N_b = N_c = 0,\ r \to \infty$:

If the bias field direction coincides with direction a (perpendicular magnetisation), then

$$\omega_{res} = \gamma\mu_0(H_0 - M_s) \tag{2.54}$$

If the bias field direction lies in the plane created by b and c (parallel magnetisation), then

$$\omega_{res} = \gamma\mu_0\sqrt{H_0(H_0 + M_s)} \tag{2.55}$$

In addition, ω_{res} also becomes anisotropic due to the anisotropy field $\mu_0\mathbf{H}_{ani}$. This introduces a third value for ω_{res} because now we distinguish between directions b and c. The exact formulas I will be using are covered in the chapter **YIG and Ga:YIG**.

2.6 FMR spectroscopy

So far I have written about the theoretical aspect of FMR. This chapter is dedicated to the common FMR setups, followed by a description of the laboratory setup I work with. (cf. [43], [44])

2.6.1 Types of FMR approaches

Cavity FMR

Historically, the first FMR setup that came around was the *cavity FMR*. It consists of a microwave source, a microwave cavity, and an electromagnet. The basic idea is that the cavity resonance occurs at fixed frequencies, while ω_{res} is "swept" through a frequency band. When ω_{res} matches the cavity resonance frequency, then the FMR signal can be observed.

In order to excite the FMR in the sample, a microwave source transmits an electromagnetic (EM) wave to the cavity. The frequency of the EM wave is chosen so that it matches the resonance frequency of the cavity. The reflected signal forms standing waves, thus leading to amplification. The sample is placed inside. Now, because of (2.54), (2.55), ω_{res} can be sweeped by applying and modulating an external field H_{ext}. The modulation is achieved by controlling the current passing through the magnets. At the resonance frequency, the FMR is excited in the whole sample, and the signal from the source is absorbed. A detector then reads this drop in signal intensity. At the FMR signal peak, the value for H_0 is measured, which concludes the experiment.

The experiment setup is relatively simple. In addition, due to the signal amplification and the global sample excitation, it is possible to find very weak FMR signals, and the measurements are very precise. However, only single FMR frequencies can be achieved.

Broadband frequency FMR

There are some other FMR spectroscopy techniques used today. One of them is the *Broadband frequency FMR*. In comparison to the cavity FMR, a *vector network analyzer*

(VNA) replaces the microwave source. Also, it uses a microstrip or coplanar waveguide for excitation. The cavity is completely omitted.

The VNA generates an alternating current (AC) signal, which is sent through the coaxial cables to the microstrip. Due to the Oersted effect, the microstrip then creates a magnetic field. The sample sits on top of the microstrip. The precession of the magnetisation around the effective field absorbs energy from the microwave field when the resonance condition is met. The output signal returns to the VNA, where the resonance is visible as a dip in the transmitted signal. The VNA allows us to sweep the signal frequency, modulate the power, and automate measurements. By sweeping both signal frequency and field strength, a multitude of FMR traces can be obtained.

The VNA FMR gives us a dataset in a great frequency window. The FMR behaviour can be monitored up to several tens of GHz. The dataset also aids in determining α_G experimentally. However, the calibration of the VNA is necessary, and the signal strength is lower without the cavity. This amounts to more preparation work and less precision.

2.6.2 FMR setup used in experiments

For the measurements, I used the VNA FMR setup. It consists of an Anritsu VectorStar MS4642B VNA, a GMW Associates BPS-85-70-EC power supply, a GMW Associates 3473-70 electromagnet, a SENIS I1A series magnetic transducer, a Keithley 2602B source meter, and a PC running thaTEC software.

The magnetic transducer measures the magnetic field H_0 at the sample location and displays the value on the connected source meter. The computer controls the power supply for the electromagnet, and therefore also the generated field H_0. The VNA excites the FMR and saves the measurement data. It can be controlled either manually or with the computer.

The waveguide in the experiment needs to meet some requirements for good performance, i.e. optimised signal transmission and FMR excitation, as well as reduced losses of any kind. This is achieved mostly by matching the impedance of the cables with the microstrip

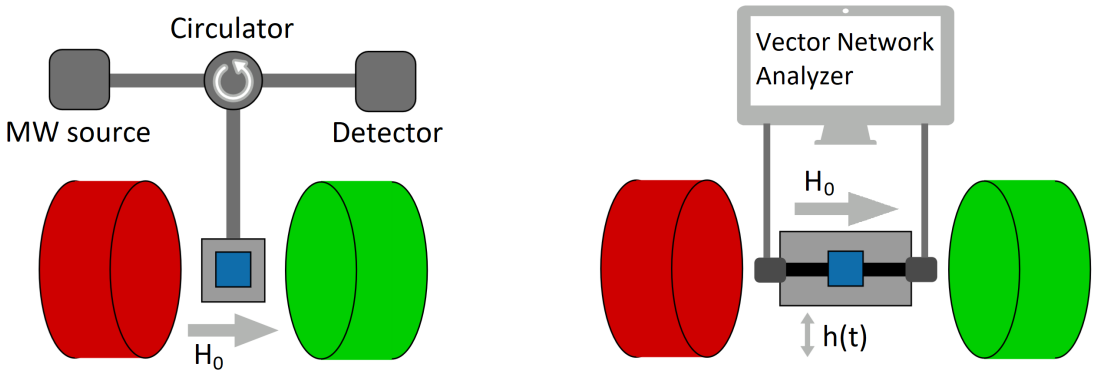

Figure 2.3: Schematic setup of FMR spectroscopy: (l.) cavity FMR, (r.) VNA FMR

and reducing the signal reflection at discontinuities. Therefore, the next chapter describes the waveguide design process.

Figure 2.4: Pictures of the FMR laboratory. (l.) The FMR workspace, including electromagnet, power supply, source meter, VNA, and computer. (u.r.) A close-up of the electromagnet and the magnetic transducer. (l.r.) A close-up of the sample holder, microstrip, and sample.

3 Waveguide design for FMR

3.1 Basic concepts of microwave engineering

3.1.1 Characteristic impedance

Consider two coupled wires connected to a voltage source. The voltage source sends a sinusoidal signal through the wires. Suppose we want to determine the voltage $V(z)$ and the current $I(z)$ along the transmission line path. This is possible either via the Maxwell equations or the Kirchhoff laws. The Kirchhoff laws, however, require lumped element equivalent circuits. The aim is to find the equivalent circuit by focussing on a small segment of the transmission line.

Assume the line segment starts at z and ends at $z+\Delta z$. Then the wire exhibits inductance L, resistance R and capacitance C, in addition to the conductance of the dielectric material G. Putting all together, the Kirchhoff laws are then applied:

$$\begin{aligned} V(z) - I(z)R\Delta z - I(z)i\omega L\Delta z - V(z+\Delta z) = 0 \\ I(z) - V(z+\Delta z)G\Delta z - V(z+\Delta z)i\omega C\Delta z - I(z+\Delta z) = 0 \end{aligned} \tag{3.1}$$

Dividing the equations by Δz and letting $\Delta z \to 0$ gives

$$\begin{aligned} \frac{dV(z)}{dz} &= -(R+i\omega L)I(z) \\ \frac{dI(z)}{dz} &= -(G+i\omega C)V(z) \end{aligned} \tag{3.2}$$

The solutions to this system of differential equations are given by a linear combination of exponential functions:

$$\begin{aligned} V(z) &= V_0^+ e^{-\gamma z} + V_0^- e^{\gamma z} = V^+(z) + V^-(z) \\ I(z) &= I_0^+ e^{-\gamma z} + I_0^- e^{\gamma z} = I^+(z) + I^-(z) \end{aligned} \tag{3.3}$$

where

$$\gamma = \alpha + i\beta = \sqrt{(R+i\omega L)(G+i\omega C)}$$

The consequent impedance of this circuit is called *characteristic impedance* Z_0. It is calculated by rewriting $I^+(z)$ with (3.2):

$$Z_0 = \frac{V^+(z)}{I^+(z)} = -(R+i\omega L)\frac{V^+}{\frac{dV^+(z)}{dz}} = \sqrt{\frac{R+i\omega L}{G+i\omega C}} \tag{3.4}$$

The characteristic impedance of free space is at around 376 Ohms.

3.1.2 Scattering parameters

Let us include a load at the end of the transmission lines, or more generally, a *2-port network*. It receives an electromagnetic signal in the form of a wave. One portion of the signal will pass through the device and get transmitted, the other part will be reflected back to the source, assuming there are no losses. This holds for both ports. In order to quantify the amount of reflection (or scattering) at the ports, the formalism of *scattering parameters* will be used. (cf. [45])

Waves going towards the ports are a_1 and a_2, their current is by definition counted positively. The letters b_1 and b_2 denote the outgoing waves, their current is counted negatively. The *reflection factor* Γ and the *transmission factor* T are defined as

$$\Gamma = \frac{b_1}{a_1} \tag{3.5}$$

$$T = \frac{b_2}{a_1} \tag{3.6}$$

For $\Gamma = 0$, there is no reflection. For $\Gamma = 1$, the incident wave is completely reflected.

Reflection occurs wherever there is an impedance mismatch. If the source impedance does not match the device impedance Z_0, or likewise, if there is another device in series with a different impedance Z_1, then they will introduce scattering. We can rewrite Γ now in terms of two impedances Z_0 and Z_1:

$$\Gamma = \frac{Z_1 - Z_0}{Z_1 + Z_0} \tag{3.7}$$

For example, the reflection in a 50 Ohms cable at an open port would be $\frac{376-50}{376+50} \approx 0.77$.

The incident signal and reflected signal inside a cable lead to a standing wave. The *voltage standing wave ratio* (VSWR) is found by dividing the maximum voltage by the minimum voltage:

$$\text{VSWR} = \frac{|V_{max}|}{|V_{min}|} = \frac{1 + |\Gamma|}{1 - |\Gamma|} \tag{3.8}$$

Finally, the transmission can be formulated via an S-matrix, which contains all scattering parameters for this network:

$$\begin{pmatrix} b_1 \\ b_2 \end{pmatrix} = \begin{pmatrix} S_{11} & S_{12} \\ S_{21} & S_{22} \end{pmatrix} \begin{pmatrix} a_1 \\ a_2 \end{pmatrix} \tag{3.9}$$

where

$$S_{11} = \frac{b_1}{a_1} = \Gamma_1, \qquad S_{22} = \frac{b_2}{a_2} = \Gamma_2 \tag{3.10}$$

$$S_{21} = \frac{b_2}{a_1} = T_{1\to 2}, \qquad S_{12} = \frac{b_1}{a_2} = T_{2\to 1}$$

dB and dBm

There are mainly two ways to designate the power reading of a signal. The first one is the dB scale, and it gives the power ratio between two signals in powers of 10. The exact formula is as follows

$$P = P_0 \cdot 10^{\frac{L_{dB}}{10}} \tag{3.11}$$

For instance, if the signal power P is 100 times bigger than P_0, then the power ratio is 100, or 20 dB. It is evident that this scale is dimensionless and only determines the relative signal strength.

The other scale is the dBm scale. It is equivalent to the dB scale, only with the difference that P_0 is a fixed value: $P_0 = 1$ mW. Thus, any power relative to P_0 has a definite power value. Take P from above, but now in dBm. 20 dBm are equal to 100 mW.

3.1.3 Skin effect

The wire electrical resistance in direct current (DC) circuits is described by the DC resistance. If we switch to alternating current (AC) circuits however, the same DC electrical resistance no longer applies to the wire. The AC resistance is found by first explaining what is called the *skin effect*. (cf. [4])

In an AC circuit, the current constantly changes direction. The magnetic fields generated inside of the wire cause an increase in resistivity, most notably in the center of the conductor. As a consequence, the center is not conductive anymore, and the charge carriers are concentrated in the hull (or skin) of the conductor. The skin depth δ describes the depth at which the current drops to 1/e of its value on the conductor surface. It can be calculated for the operating circuit frequency ω

$$\delta = \sqrt{\frac{2\rho}{\omega\mu\mu_0}} \tag{3.12}$$

where ρ is the resistance and μ is the magnetic permeability of the material. In radio frequency (RF) applications it is advisable to use trace thicknesses $d < 5\delta$. For $d < 3\delta$, the skin effect is already negligible. [4] (see fig. 3.1)

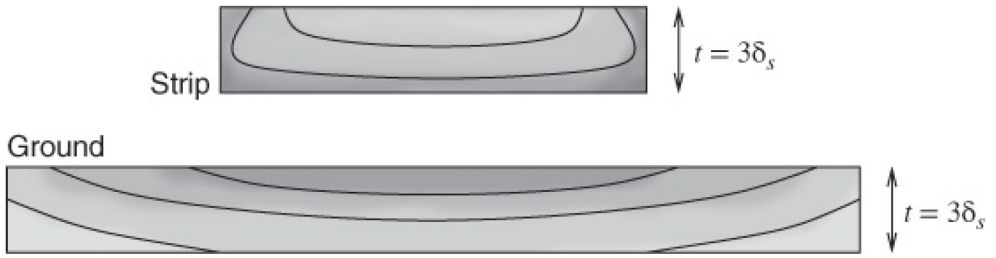

Figure 3.1: Transverse current density shown in the cross section of the strip and ground plane of a microstrip. Dark shading indicates higher current density. Taken from [4].

3.2 Waveguides for microwave signals

Waveguides are elements in which waves can propagate in the desired direction. A prime example is the microstrip line, consisting just of a substrate, a conductor strip on top and a ground plane on the bottom. Conveniently, the characteristic impedance is determined by very few parameters, namely the trace width w, the substrate height h, the substrate dielectric constant ϵ_r, and to a lesser degree, the trace height t. This simplifies the impedance matching. If the microstrip cross section geometry does not change along the transmission line, then the waveguide retains good signal integrity.

3.2.1 Propagation in waveguides

When speaking about waveguides, it makes sense to step away from the concept of current and voltage. Rather, we tend to look at EM waves. As such, I will only refer to current and voltage if it is deemed necessary.

Suppose we want to send a pulse signal through a coaxial line. (cf. [46]) The voltage applied to the two conductors creates an electric field E. The E field lines are mostly directed from the center conductor to the outer conductor. Since they are in the transversal plane perpendicular to the wave propagation, it is referred to as E_t. Furthermore, the current flows along the line, so E also has a longitudinal component E_l. However, in coaxial lines the longitudinal component is much smaller than the transverse component, $E_l \ll E_t$. The current generates a magnetic field H, where again the transverse component is considerably bigger than the longitudinal, $H_l \ll H_t$. In general, fields where $E_l \ll E_t$ and $H_l \ll H_t$ are called *transverse electromagnetic modes* (TEM).

In comparison to coaxial lines, the cross sectional structure of the microstrip is inherently asymmetrical. The conductor strip is located between a substrate and air, and therefore, the permittivity of both materials need to be taken into account. The EM field is affected by this asymmetry as well. As a result, the longitudinal components E_l and H_l are not as small anymore. In this case we speak of *quasi TEM modes* (QTEM). Note that the longitudinal components increase with the frequency, but broadly speaking, the resulting modes are very close to being TEM.

3.2.2 Multiple signal modes

The EM field deviates from the QTEM mode at hand under certain conditions. [46] First, in the presence of another conductor. The conductors establish two coupling modes, the *even mode* and *odd mode*, which represent the same or opposite voltage polarity in the lines, respectively. The coupling leads to distinct characteristic impedances for each mode.

Second, if the conductor width w is $\lambda/2$ or greater. When this condition is met, the *lowest-order transverse resonance* occurs. The equivalent circuit is a resonant transmission line of length $w' = w + 2d$, where $d = 0.2h$ and h is the substrate height. The cut-off frequency is given by [4]

$$f_{\mathrm{CT}} = \frac{c}{\sqrt{\epsilon_r}(2w + 0.8h)} \tag{3.13}$$

where c is the speed of light in free space, and ϵ_r is the substrate dielectric constant.

Lastly, the conditions for exciting transverse electric (TE) and transverse magnetic (TM) modes [47] will be covered specifically for the microstrip structure.
Collin and Vendelin obtained the cut-off frequency of the lowest-order TE wave at

$$f_e = \frac{c}{4h\sqrt{\epsilon_r - 1}} \tag{3.14}$$

The TM mode limitation is calculated separately for wide and for narrow microstrip lines:

$$f_m = \frac{75}{H\sqrt{\epsilon_r - 1}}, \quad \text{wide microstrip} \tag{3.15}$$

$$f_m = \frac{106}{H\sqrt{\epsilon_r - 1}}, \quad \text{narrow microstrip} \tag{3.16}$$

where f_m is in GHz and $H = h$ in mm.

All of the above modes, if they need to be avoided, are coined as *spurious modes*. The propagation velocity generally differs for each mode, causing a signal to stretch and deteriorate with time. If the propagation velocity of two modes is similar, then they couple strongly. This is called *parasitic coupling*. (though in some instances such as bandpass filters, it is desired to couple the conductors with one another) To sum it up, the undesired modes disrupt the performance and should be prevented by careful design of the waveguide.

3.3 Design of microstrip lines for FMR studies

This chapter is dedicated to the actual design of the waveguide. It lists all the restrictions the FMR setup imposes on the waveguide geometry. First of all, we consider the requirements for transmission lines and substrates employed in FMR experiments and make a decision based on their feasibility and/or availability. The waveguide behaviour will then be analysed in the microwave frequency spectrum (up to about 40 GHz). For performance optimisation, the effect of discontinuities and transitions will be elucidated as well.

3.3.1 Types of waveguides and substrates

Ever since the evolution of the stripline, more and more transmission line structures emerged. (cf. [48]) They differ in field modes, range of characteristic impedance and operating frequencies. The planar transmission line structures can be broadly categorised in field modes. Some completely non-TEM lines are the imageline and the finline. The stripline and coaxial line represent a part of the pure TEM line group. Other structures like microstrip, coplanar waveguide and differential line exhibit a QTEM mode.

Conditions for FMR

As far as field modes go, the TEM, QTEM and TM modes can excite FMR. The cable impedance is 50 Ohms, which Z_0 should match. The operating frequencies range from around 1 GHz to 20 GHz. The cable connectors are required to be nonmagnetic, so that

they do not affect the measurements. Finally, the transmission line should be accessible for sample placement.

Choice of transmission line

The microstrip and the coplanar waveguide both fulfill the criteria for FMR experiments. As was said, they are QTEM lines. Their Z_0 is tunable in the range of [10,110] Ohms (microstrip) and [40,110] Ohms (coplanar waveguide). Lastly, the microstrip can operate well up to 80 GHz, while the frequency limit for the coplanar waveguide is even higher. The microstrip design was chosen for this thesis.

Choice of substrate

There are usually multiple questions that need to be answered when choosing the substrate material. But, due to the simplicity of the FMR setup compared to other more sophisticated experiments, requirements for mechanical stability and thermal expansion coefficient, among other things, are very basic. What is important are the dielectric constant ϵ_r and the operating frequency range. The RT/duroid 6002 laminate from the Rogers Corporation has been selected as the waveguide substrate. The key properties are listed below.

- Dielectric constant (ϵ_r) of 2.94 +/- 0.4
- Low thermal coefficient of ϵ_r at 12 ppm/°C
- Dissipation factor of .0012 at 10 GHz
- Low Z-axis coefficient of thermal expansion at 24 ppm/°C

3.3.2 Microstrip design

There is no one exact formula for the characteristic impedance of a microstrip, which is, to some extent, frequency dependent. However, there exist formulas for up to several GHz which are accurate to at least 1 %. [49] These assume a static TEM field. The equations can be modified to predict the Z_0 behaviour in higher frequencies.

As it turns out, at low microwave frequencies, ϵ_{eff} and Z_0 are strongly related to the microstrip aspect ratio, $u = w/h$. Hammerstad and Jensen [50] found closed formulas for both of them:

$$\epsilon_{eff} = \frac{\epsilon_r + 1}{2} + \frac{\epsilon_r - 1}{2}\left(1 + \frac{10h}{w}\right)^{-a \cdot b} \tag{3.17}$$

where

$$a(u)_{|u=w/h} = 1 + \frac{1}{49}\ln\left[\frac{u^4 + (u/52)^2}{u^4 + 0.432}\right] + \frac{1}{18.7}\ln\left[1 + \left(\frac{u}{18.1}\right)^3\right] \tag{3.18}$$

$$b(\epsilon_r) = 0.564 \left[\frac{\epsilon_r - 0.9}{\epsilon_r + 3}\right]^{0.053} \tag{3.19}$$

and

$$Z_0(u) = \frac{Z_{01}(u)}{\sqrt{\epsilon_{eff}}} \tag{3.20}$$

where $Z_{01}(u)$ denotes the characteristic impedance in free space:

$$Z_{01}(u) = Z_0(u)_{|\epsilon_r=1} = 60 \ln \left[F_1/u + \sqrt{1 + (2/u)^2}\right] \tag{3.21}$$

where

$$F_1 = 6 + (2\pi - 6) \exp\left[-(30.666/u)^{0.7528}\right] \tag{3.22}$$

Fortunately, there are many websites offering the calculation of ϵ_{eff} and Z_0 for simple microstrips, so it is not necessary to calculate them „by hand“.

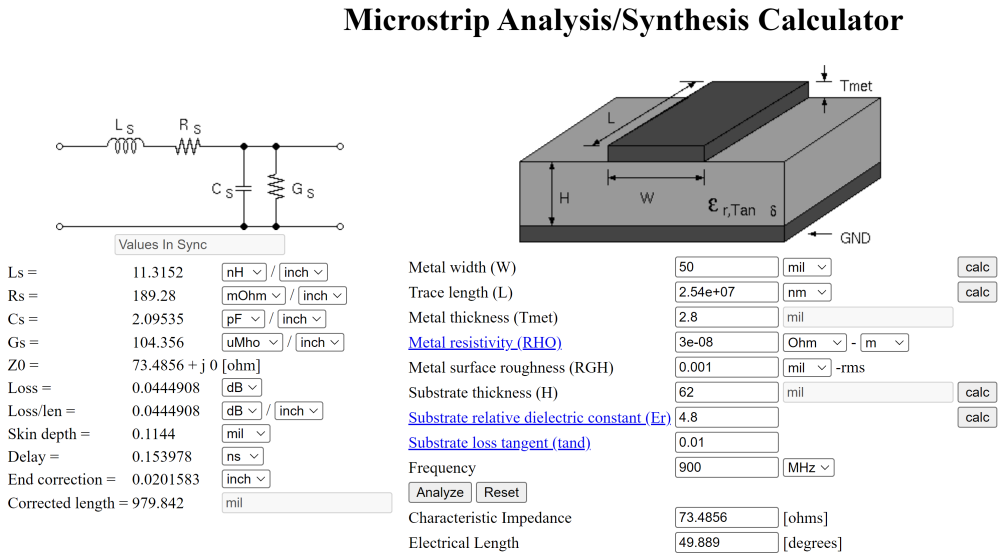

Figure 3.2: Online microstrip calculation tool. [5]

Thus, upon finding the aspect ratio u, a balance between different losses is to be achieved. On one hand, narrow transmission lines cause conductor losses due to the increasing line resistance. This problem is exacerbated by the skin effect at higher frequencies. On the other hand, wider transmission lines lead to spurious modes and parasitic coupling. In addition, with greater h, the radiation losses increase as well. (cf. [51]) A lower limit for w is set by the width of the connector pin.

3.3.3 Discontinuities in the trace line

The microstrip and sample are fixed between the magnet poles. For a stronger excitation under parallel magnetisation, the EM wave in the waveguide should propagate along the externally applied magnetic field H_{ext}. The reason is simple: The QTEM mode ensures

that $h(t)$ is virtually completely confined to the transverse plane, which in turn excites the FMR according to (2.48).

The most simple approach to the microstrip design is then to leave it as a straight line. The cables are connected to the printed circuit board (PCB) with right-angle adapters. However, the adapters introduce more separation between the magnet poles. This has two consequences. First, the magnetic field will become less homogeneous. Second, the field in the center will be weaker. That implies a lower frequency limit in the broadband FMR measurements according to (2.54), (2.55). Also note that adapters generally increase scattering.

I propose a waveguide with a different shape. The presence of transmission line bends in the PCB shall replace the angle adapters. Hence, the line shape resembles that of the letter „U“. In general, bends affect the characteristic impedance due to changes in inductance of the trace. For example, in a right-angle unmitred bend the charges accumulate at the corners. [52] Some tweaks to the bends are necessary to suppress those undesired effects. I will shortly compare two kinds of bends, the radial bend and the mitred bend.

Radial bends can be a great way to connect circuit elements at any arbitrary angle. As a general rule of thumb, the radius of the bends should be greater than about $3w$, and $5w$ in higher frequencies. [52]

Another kind of bend represent the mitred bends. There have been reports [52] of optimal mitre values to mitigate the otherwise increased inductance. However, the mitre value has been optimised for alumina substrates and others where ϵ_r is hovering around 10. In comparison, the RT/duroid 6002 laminate has a reported ϵ_r of 2.94. Thus, the difference between the radial and the mitred bend needs to be examined.

3.3.4 Transitions between two waveguide geometries

Until now, a lot of ground has been covered in the FMR microstrip design. One of the last steps is the incorporation of transitions. (cf. [53]) One purpose of waveguide transitions is to exploit the benefits of each waveguide type that is used. In the chapter **Types of waveguides and substrates** I concluded that the microstrip and the coplanar waveguide (CPW) meet the requirements for FMR spectroscopy.

Advantages of the CPW

The CPW structure [6] consists of two ground planes and one conductor evenly placed between them, all mounted on the top of a substrate. The ground planes serve to minimise the radiation losses that would otherwise occur with the microstrip design. The reason is that the field is mainly localised between the conductive surfaces instead of inside the substrate.

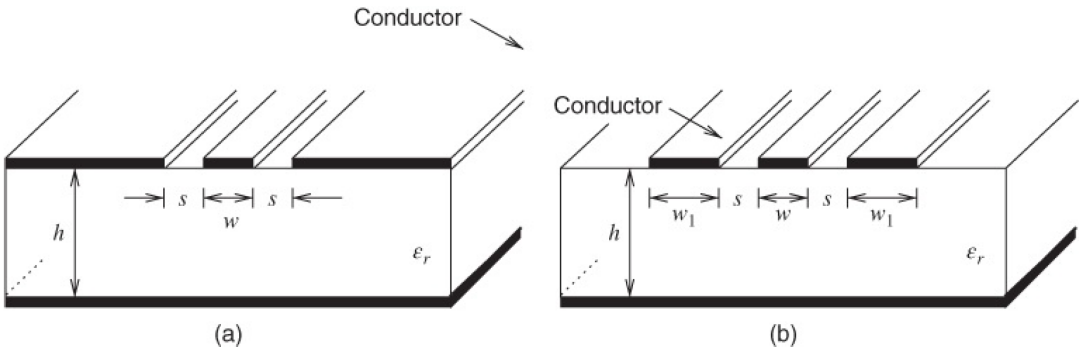

Figure 3.3: Cross-section of a CPW: a) GCPW b) FG-GCPW. Taken from [6].

The CPW structure can also be modified by adding a ground plane to the bottom which makes it a grounded coplanar waveguide (GCPW). The extra ground plane shields the EM field from outside noise and adds mechanical stability to the PCB. In other applications, it could be used as a heatsink as well. Despite shielding the CPW, the ground plane also enables higher-order modes. The side ground planes and the bottom ground plane effectively behave like a resonant cavity. The trace strongly couples to the resonant cavity and excites spurious modes. This effect becomes more noticeable the wider the side ground planes are.

Via fences

Sain and Melde [54] reported shifts in resonance frequencies of the resonant cavities when implementing arrays of vias, also commonly known as *viafences*. The vias are placed on the side ground planes, and the array is parallel to the trace. The paper focusses on via placement parameters. They found that a via spacing of $\lambda/4$ prevents higher-order modes up to the maximum operating frequency, where λ is its corresponding wavelength. The reported via spacing applies to the centre-to-centre distance between trace and vias, as well as between two vias.

Transition from CPW to microstrip

A possible CPW-microstrip transition design was proposed by Jin and Vahldieck. [7] (see fig. 3.4) It works in the 0-40 GHz frequency band and utilises step changes in gap width. In contrast, I gradually increase the gap in my waveguide by means of radiused ground plane corners.

3.4 Simulation of the microstrip lines

For the EM simulation I use the program COMSOL. COMSOL offers many physics modules and can combine them in COMSOL Multiphysics. The RF module features field solutions and scattering parameters for waveguides, antennas and the like, operating at RF.

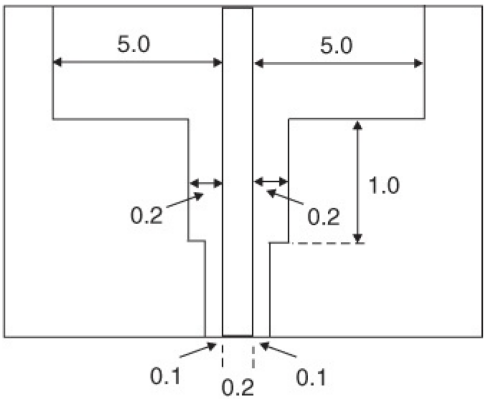

Figure 3.4: Transition from CPW to microstrip. Dimensions are given in mm. Adopted from [7].

Creating the geometry

To start off, I choose the Radio Frequency physics and tick the study „Electromagnetic Waves, Frequency Domain“. This allows me to do a frequency sweep when calculating the EM fields. For the geometry, I define a sphere that will mark the boundary of the system. The waveguide is placed inside of it. The dimensions are listed in table 3.1.

width	depth	height	trace width	gap
28 mm	30 mm	0.381 mm	0.835 mm	0.225 mm
via radius	via spacing	sample space	radius	mitre
0.075 mm	0.75 mm	$\geq$ 8 mm	4.5 mm	0.472 mm

Table 3.1: Dimensions of the designed waveguide (radiused and mitred)

Scattering boundary

The unintended reflection of EM waves at the boundary layer leads to distorted results in the simulation. Thus, there needs to be some kind of scattering at the boundary. The scattering of EM waves can be achieved in two ways: *scattering boundary conditions* (SBC) or *perfectly matched layers* (PML). While SBCs are easier to implement, PMLs absorb incident EM waves even at more oblique angles than SBCs. [8] (see fig. 3.5) The settings are polynomial stretching, PML scaling factor 1, and PML scaling curvature parameter 3.

Materials

The materials are assigned individually. I set the sphere and the PMLs as air and the substrate as RT/duroid 6002 laminate. All conductive surfaces are treated as *perfect electric conductors* (PEC).

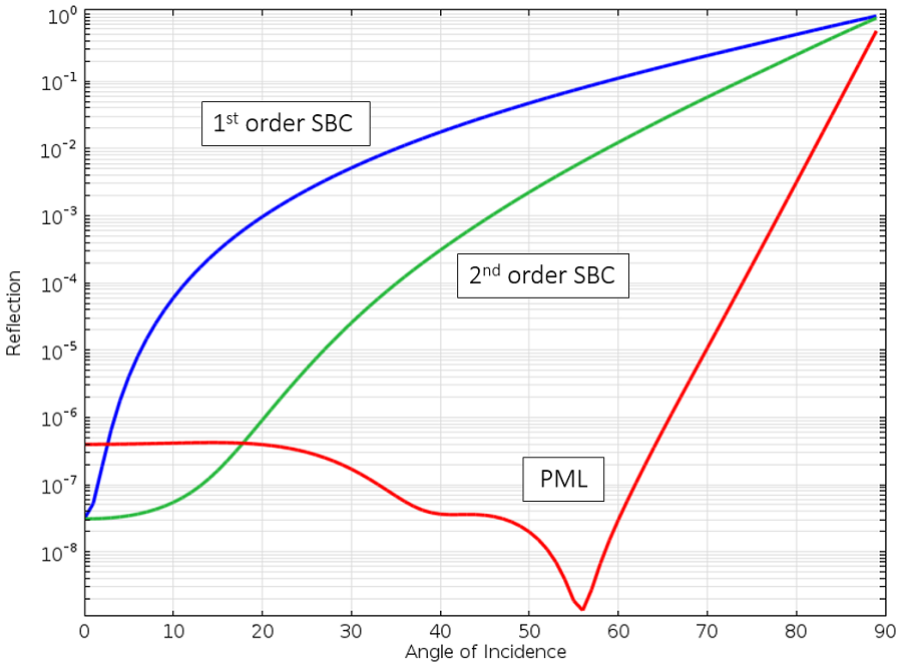

Figure 3.5: Reflection vs angle of incidence for SBCs and PMLs. Taken from [8].

Lumped ports

Lumped ports are necessary in order to excite and terminate a signal at given points in the geometry. There are a handful of different lumped ports in COMSOL. I choose uniform lumped ports with the settings: terminal type cable, $P_0 = 1$ mW, $Z_{ref} = 50$ Ohms.

Mesh, Solver

The mesh is physics-controlled, with a normal element size. COMSOL automatically creates a swept mesh for the PMLs. The frequency sweep is in the range [1 GHz, 20 GHz] in increments of 1 GHz.

4 Gallium doped Yttrium Iron Garnet

4.1 Introduction to Magnonics

Magnonics is a growing research field [19] enabling an alternative approach to traditional computation technology. It works with magnons - quanta of spin waves - as the main data carrier. Spin waves (SW) are the propagating collective motion of magnetic moments, and they form a family of functions solving the LLG equation. They can be used as an information medium, which would have several advantages over electric current [20]:

Higher operating frequencies

The clock rate for a modern computer lies in the GHz range. The frequency limit is set by the circuit temperature. An increase in temperature eventually leads to artifacts in data processing, and in the worst case, to failure. On the other hand, signals in the THz range could be accomplished with SWs. The Brillouin zone of the material and the applied magnetic field determine the upper frequency boundary in magnonics.

Decreased heat dissipation

The electric current generates Joule heating due to the finite line resistance of the wires. This necessitates external cooling, adding to the overall power consumption. In magnonic circuits there is no current involved in the first place. The source of losses is primarily given by the spin wave damping.

Scalability

With the goal of ever increasing processing speed, the engineers strive to keep up with Moore's law. The chips should house more transistors, therefore each transistor becomes smaller. Recent progress revealed that sub 10-nm transistors are possible using 2D materials [55], but in those dimensions quantum mechanical effects heavily influence the chip design. [56] [57] Workarounds were and will be needed down the line. In comparison, it was reported that the fabrication of high quality magnonic materials in the nm range is possible. [21] The minimum size of a magnonic circuit element is given by the lattice constant of the material. A workaround in chip architecture is not required.

Nonboolean states

Binary computers process information as bits, a bit either represents the state 0 or 1. Wave-based computing, though, allows for a nonboolean state by taking the wave phase into account. Considering the greater information density of SWs, multiplexing becomes intrinsically possible, hinting at the idea of expanding into parallel computing.

It is evident that most of the magnonics advantages are reflected in the material properties. To summarise, a magnonic material for competitive computational power should exhibit thermal stability (phase transition temperature above 300 K), high structural quality, small Gilbert damping, SW frequencies in the GHz range, high SW velocities, and lastly, allow for controlled nanofabrication. [58]

4.2 Magnetostatic Spin Waves

A selection of materials meet the aforementioned criteria appreciably. Among them are Permalloy, CoFeB composites, Heusler half-metallic compounds and single-crystal YIG. [9] YIG is a ferrimagnetic insulator with the lowest known Gilbert damping. This ensures that the lifetime of SWs is two orders greater than in permalloy, for example. But until recently, YIG could only be fabricated in the µm scale. Analogous to multimoding in wide transmission lines, µm-thick YIG conduits are prone to spurious modes.

It has been shown that in 44 nm thick, 50 nm wide YIG conduits with an aspect ratio reaching 1, the waveguide now supports single-mode operation. [59] The dispersion relation becomes exchange dominated, and the spin wave modes get unpinned, which causes a quasi uniform SW mode profile as opposed to a sinusoidal profile in µm wide conduits. Furthermore, the total energy is lowered, and by that, the frequency as well. Hence, the modes are quantised on the frequency axis. The quantisation prevents the SW mode from scattering into higher width modes. In principle, three distinct geometries can be realised. (see fig. 4.1) While the backward volume magnetostatic spin waves (BVMSW) and the magnetostatic surface spin waves (MSSW) exhibit strong anisotropy [22], the forward volume geometry (FVMSW) would allow the propagation of isotropic exchange SWs. The caveat is the necessary high external magnetic fields to fully magnetise YIG out of plane (OOP). The reason is that the magnetic easy axis in YIG is located in plane (IP). In addition, the generated SWs are comparably slow at about 0.2 µm/ns. [22]

In comparison, hexaferrites have the advantage of a perpendicular magnetic anisotropy (PMA), which opens access to controllable spin wave transport in complex 2D magnonic networks and the facilitation of isotropic SW propagation. Naturally, a material with intrinsic PMA would not require high external OOP fields to reach its saturation magnetisation and operate in the forward volume geometry.

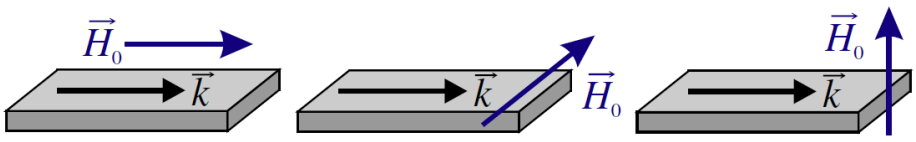

Figure 4.1: Three spin wave geometries: (f.l.t.r) backward volume, surface, forward volume. Adopted from [9].

4.3 Gallium doped Yttrium Iron Garnet

Through state-of-the-art material engineering, YIG-substituted materials might serve the purpose of waveguides better than pure YIG. Studies have been conducted on a number of candidate materials, including Bi:YIG [23] [26], Bi:LuIG [27], TmIG [24] and Mn:YIG [25]. By changing the lattice mismatch of the film and the substrate, the easy axis is effectively shifted into OOP. This renders the films with PMA. Therefore, the magnitude of the external field can be kept as low as some mT in the forward volume geometry. However, the aforementioned materials typically demonstrate higher damping and a broad range of relaxation parameters across the measurement geometries.

In the 1970s and 1980s, Gallium doped YIG has been researched [28], but the limitations of low structural quality and thickness brought further studies to a halt. Now considering the progress in ultrathin film fabrication [2] [29], interest in Ga:YIG for SW applications has reemerged. The Ga^{3+} ions substitute the magnetic Fe^{3+} ions, leading to partial or even full substitution in both magnetic sublattices, octahedral and tetrahedral. The dispersion relation of Ga:YIG is exchange-dominated, hence the SWs are expected to be highly isotropic. Also, the SW group velocity for exchange waves is inversely proportional to M_s, so the magnetic compensation in Ga:YIG should in turn increase the SW velocities.

I will compare the Gilbert damping α_G, the saturation magnetisation M_s and the anisotropy fields in samples of single-crystal YIG and Ga:YIG. The samples are grown by liquid phase epitaxy (LPE).

4.4 Computation of the magnetic parameters

4.4.1 Formulas for the resonance frequency

In their work, Bobkov and Zavislyak examined the effect of substrate and crystal orientation on the subsequent anisotropy energy in epitaxial ferrite films. [1] They were able to deduce the frequency dependent components of the permeability tensor $\hat{\mu}$. With this, they also found the FMR resonance frequencies. Böttcher et al. then summarised the FMR solutions in two separate equations (in SI units) [2]:

For IP FMR:

$$f^2 = \left(\frac{\gamma\mu_0}{2\pi}\right)^2 [(H_i + H_{A1} + M_s)(H_i + H_{A2}) - H_{A3}^2] \tag{4.1}$$

For OOP FMR:

$$f^2 = \left(\frac{\gamma\mu_0}{2\pi}\right)^2 [(H_i + H_{A1})(H_i + H_{A2}) - H_{A3}^2] \tag{4.2}$$

where $H_i = H_0 - M_s$. Note that the circular frequency ω has been substituted by the linear frequency $f = \omega/2\pi$.

The samples analysed in this work are grown on *Gadolinium Gallium Garnet* (GGG), with the crystal orientation either (111) or (001). Depending on the orientation, the

calculation of the magnetic parameters will differ a bit. Therefore I will cover GGG(111) and GGG(001) in separate sections.

4.4.2 Parameters for Gadolinium Gallium Garnet(111) substrates

Resonance frequency

Consider YIG and Ga:YIG films grown on GGG(111). The fig. 4.2 shows the crystallographic directions of YIG and Ga:YIG films with respect to the substrate surface. The H_{A1}, H_{A2} and H_{A3} are given in table 4.1. The components consist of three main anisotropy fields: the cubic field $H_c = K_c/\mu_0 M_s$, the first order uniaxial field $H_{u1} = 2K_{u1}/\mu_0 M_s$, and the second order uniaxial field $H_{u2} = 4K_{u2}/\mu_0 M_s$. The latter two arise from the uniaxial strain present in the crystal and effectively contribute to the noncubic anisotropy.

	H_{A1}	H_{A2}	H_{A3}
IP: **H** $\parallel [1\bar{1}0]$	$-\frac{K_c}{\mu_0 M_s} - \frac{2K_{u1}}{\mu_0 M_s}$	0	$-\sqrt{2}\frac{K_c}{\mu_0 M_s}$
IP: **H** $\parallel [11\bar{2}]$	$-\frac{K_c}{\mu_0 M_s} - \frac{2K_{u1}}{\mu_0 M_s}$	0	0
OOP: **H** $\parallel [111]$	$-\frac{4}{3}\frac{K_c}{\mu_0 M_s} + \frac{2K_{u1}}{\mu_0 M_s} + \frac{4K_{u2}}{\mu_0 M_s}$		0

Table 4.1: The parameters H_{A1}, H_{A2} and H_{A3} for iron garnet/GGG(111). Adopted from [1] [2].

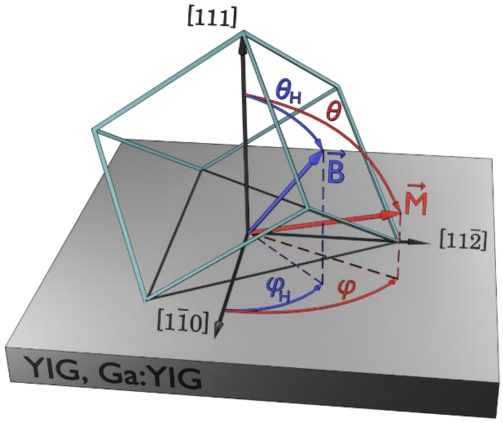

Figure 4.2: Crystallographic axes of YIG/GGG(111) and Ga:YIG/GGG(111). Adopted from [2].

Together with equations (4.1), (4.2), we then arrive at the specific formulas:

$$f_{||}[1\bar{1}0] = \frac{\gamma\mu_0}{2\pi}\sqrt{H^{||}(H^{||} - H_c - H_{u1} + M_s) - 2H_c^2} \tag{4.3}$$

$$f_{||}[11\bar{2}] = \frac{\gamma\mu_0}{2\pi}\sqrt{H^{||}(H^{||} - H_c - H_{u1} + M_s)} \tag{4.4}$$

$$f_{\perp} = \frac{\gamma\mu_0}{2\pi}(H^{\perp} - \frac{4}{3}H_c + H_{u1} + H_{u2} - M_s) \tag{4.5}$$

Parameters γ, H_c, M_{eff} and H_{u2}

The parameters γ and $M_{eff} := M_s - H_c - H_{u1}$ are fitted simultaneously for the $[11\bar{2}]$ direction. (see (4.4)) Since (4.3) only differs by $-2H_c^2$, the values γ and M_{eff} are fixed, and H_c is calculated from the $[1\bar{1}0]$ direction. H_{u2} can be deduced from the OOP fit, according to (4.5).

4.4.3 Parameters for Gadolinium Gallium Garnet(001) substrates

Resonance frequency

Ferrite films on GGG(001) have a different set of IP crystallographic axes. (see fig. 4.3) They are measured along [100] (along the side) and $[1\bar{1}0]$ (diagonally). The H_{A1}, H_{A2}, H_{A3} are listed in table 4.2.

The equations for f are listed in the following.

$$f_{||}[1\bar{1}0] = \frac{\gamma\mu_0}{2\pi}\sqrt{(H^{||} - 2H_c)(H^{||} + H_c - H_{u1} + M_s)} \tag{4.6}$$

$$f_{||}[100] = \frac{\gamma\mu_0}{2\pi}\sqrt{(H^{||} + 2H_c)(H^{||} + 2H_c - H_{u1} + M_s)} \tag{4.7}$$

$$f_{\perp} = \frac{\gamma\mu_0}{2\pi}(H^{\perp} + 2H_c + H_{u1} + H_{u2} - M_s) \tag{4.8}$$

	H_{A1}	H_{A2}	H_{A3}
IP: **H** || [100]	$\frac{2K_c}{\mu_0 M_s} - \frac{2K_{u1}}{\mu_0 M_s}$	$\frac{2K_c}{\mu_0 M_s}$	0
IP: **H** || $[1\bar{1}0]$	$\frac{K_c}{\mu_0 M_s} - \frac{2K_{u1}}{\mu_0 M_s}$	$-\frac{2K_c}{\mu_0 M_s}$	0
OOP: **H** || [001]	$2\frac{K_c}{\mu_0 M_s} + \frac{2K_{u1}}{\mu_0 M_s} + \frac{4K_{u2}}{\mu_0 M_s}$		0

Table 4.2: The parameters H_{A1}, H_{A2} and H_{A3} for iron garnet/GGG(001). Adopted from [1] [2].

Parameters γ, H_c, $\tilde{M}_{eff}$ and H_{u2}

The parameters γ, H_c and $\tilde{M}_{eff} := M_s - H_{u1}$ are fitted simultaneously. This can be done for **H** || [100], or equivalently for **H** || $[1\bar{1}0]$. H_{u2} follows from (4.8), similar to the GGG(111) evaluation.

4.4.4 Damping parameters

Patton reports that the FMR linewidth ΔH is proportional to the resonance frequency $f(H)$. [60] According to [61] [43], the formula is

$$\mu_0\Delta H = \mu_0\Delta H(0) + \frac{\alpha_G 4\pi f}{\gamma} \tag{4.9}$$

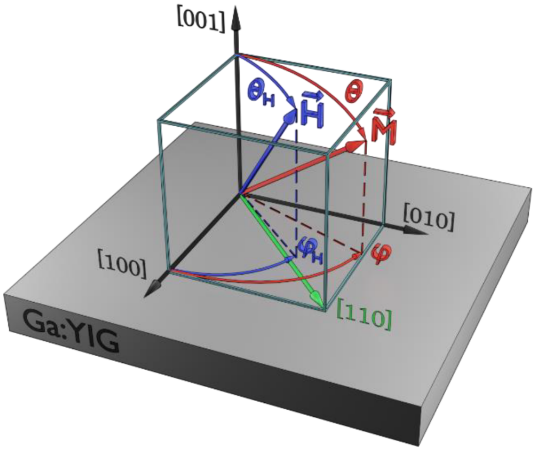

Figure 4.3: Crystallographic axes of YIG/GGG(001) and Ga:YIG/GGG(001). Adopted from [2].

where $\mu_0\Delta H$ is the full width at half maximum (FWHM) of $H(f)$, and $\mu_0\Delta H(0)$ is the *inhomogeneous linewidth broadening*.

Kalarickal et al. also reported the conversion from Δf acquired through the broadband VNA FMR to the desired ΔH [43]:

$$\mu_0\Delta H = \frac{2\pi\Delta f}{\gamma P_A(f)} \tag{4.10}$$

where $P_A(f) = \sqrt{1+\left(\frac{\gamma\mu_0 M_s}{4\pi f}\right)^2}$. However, this relation was derived for YIG samples, where $|H_c|, |H_{u1}| \ll M_s$. [2] derived the relation for each IP configuration separately, including the anisotropy fields. They are summarised in the table 4.3.

Substrate	Direction of **H**	$\mu_0\Delta H$ (recalculated from Δf)
GGG(111)	**H** $\parallel [1\bar{1}0]$	$\frac{8\pi^2\Delta f \cdot f_{\parallel}[1\bar{1}0]}{\mu_0\gamma^2(2H^{\parallel}-H_c-H_{u1}+M_s)}$
	H $\parallel [11\bar{2}]$	$\frac{8\pi^2\Delta f \cdot f_{\parallel}[11\bar{2}]}{\mu_0\gamma^2(2H^{\parallel}-H_c-H_{u1}+M_s)}$
GGG(001)	**H** $\parallel [1\bar{1}0]$	$\frac{8\pi^2\Delta f \cdot f_{\parallel}[1\bar{1}0]}{\mu_0\gamma^2(2H^{\parallel}-H_c-H_{u1}+M_s)}$
	H $\parallel [100]$	$\frac{8\pi^2\Delta f \cdot f_{\parallel}[100]}{\mu_0\gamma^2(2H^{\parallel}+4H_c-H_{u1}+M_s)}$

Table 4.3: The expressions for the linewidth $\mu_0\Delta H$ for each IP configuration of Ga:YIG, recalculated with the experimental Δf. Adopted from [2].

5 Results and discussion

5.1 Characterisation of the microstrip line

In order to measure FMR signals, we decided to use microstrip lines. The uniformity of the magnetic field is crucial in FMR experiments, therefore the spacing between the magnet poles should be minimised by the design of the microstrip. We named this special microstrip the *U waveguide*. There are two ways to achieve this, by using radiused and mitred traces.

The following simulation results show the performance of the radiused and the mitred version of the microstrip. The data in the plots is distinguished by colour, representing the radiused (orange) and the mitred (green) version of the U waveguide.

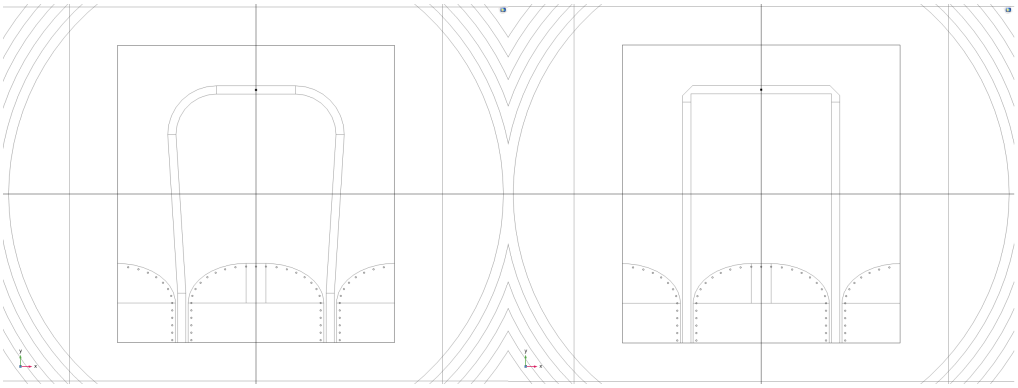

Figure 5.1: A top view of the simulated waveguides: (l.) radiused, (r.) mitred. The sample would be placed on the middle trace between the bends. The little dot in the middle trace indicates the evaluation point for the magnetic field.

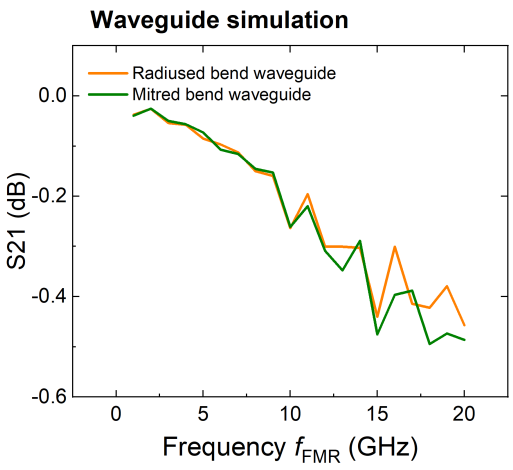

(a) The S21 parameter calculated in the COMSOL simulation for the radiused (orange) and mitred (green) bend waveguide.

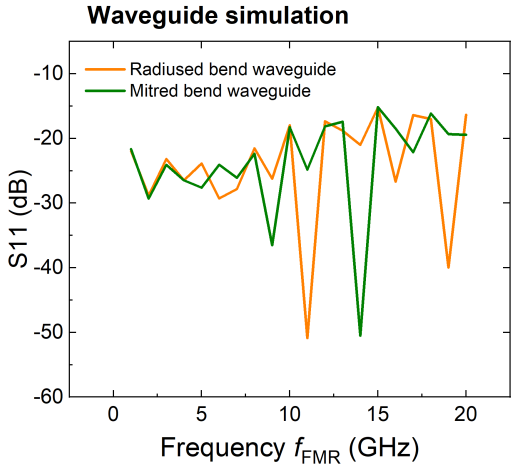

(b) The S11 parameter calculated in the COMSOL simulation for the radiused (orange) and mitred (green) bend waveguide.

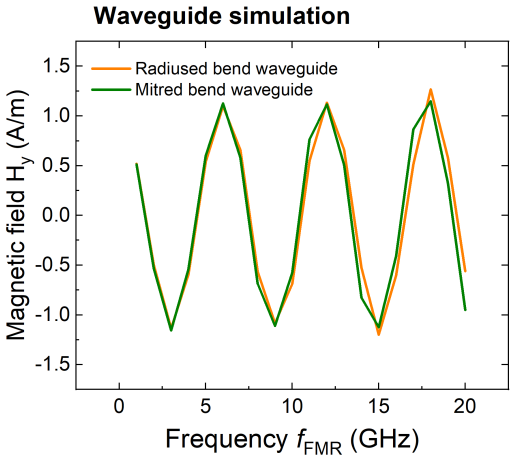

(a) The perpendicular magnetic field component H_y calculated in the COMSOL simulation for the radiused (orange) and mitred (green) bend waveguide.

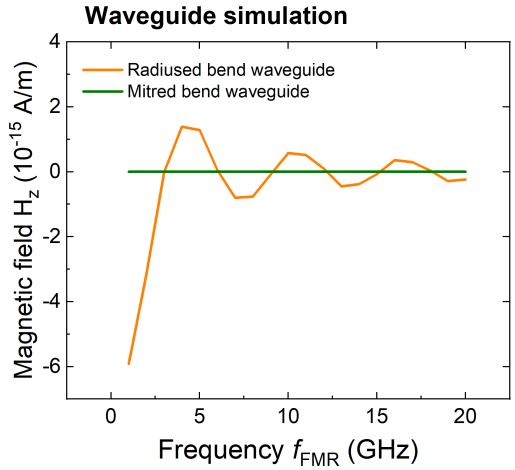

(b) The perpendicular magnetic field component H_z calculated in the COMSOL simulation for the radiused (orange) and mitred (green) bend waveguide.

Note that $H_z \ll H_y$ at the evaluation point for the radiused bend, while H_z completely vanishes for the mitred bend. (see fig. 5.3a, 5.3b) Due to the similar results, it is expected that their performance is comparable in real measurements. The radiused version has been chosen and was made by CIBEL.

The scattering parameters for the manufactured U waveguide and a commercial GCPW were acquired with the VNA in three bias fields, $H = [0, 0.1, 0.84]$ T. This was done to examine the effect of a magnetic field on the signal propagation and integrity. Furthermore, due to the use of right angle adapters, the GCPW holder is wider than the holder for the U waveguide. As a result, the spacing between the magnet poles is greater for the GCPW, therefore decreasing the available maximum field to $H_{max} = 0.84$ T.

In the case of the U waveguide, the maximum field is $H_{max} = 1.10$ T. To compare the waveguides, both of them were measured at the same fields. In addition, the U waveguide was characterised at different input powers, [0, -15, +15] dBm, in order to check the power dependency of the signal. The VNA was calibrated at the respective power level together with the cables, and for the GCPW, also with the right angle adapters.

The figures below show the comparison of the simulation (orange) vs measurement (blue) of the U waveguide, plotted in Origin.

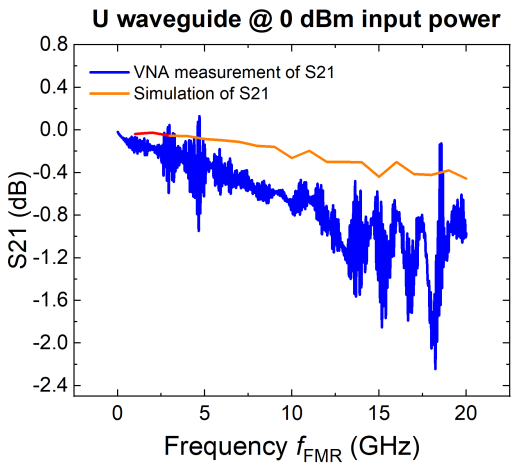

(a) A comparison of the S21 parameters acquired through the VNA measurement (blue) and the simulation (orange).

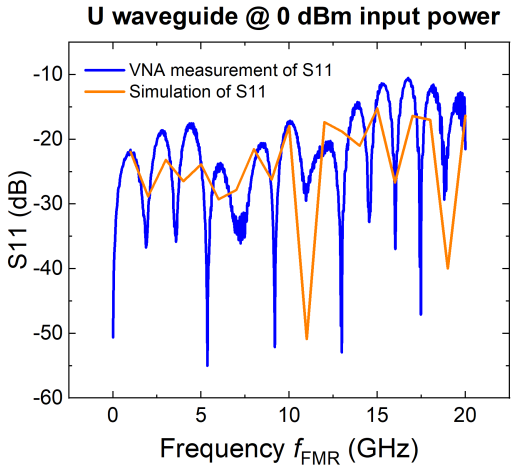

(b) A comparison of the S11 parameters acquired through the VNA measurement (blue) and the simulation (orange).

The VNA data shows that the real performance of the U waveguide is worse than the simulation results. In the observed frequency range, the simulation data of S21 proves to be mostly an upper bound for the measured data, with the exception of the peaks at around 5 GHz and 18 GHz. Additionally, the measurement data displays oscillations in signal strength between 11 GHz and 20 GHz, which are not represented in the simulations. The origin of these oscillations is thought to be radiation loss, which is inherent to the microstrip design. At higher frequencies, the radiation losses are expected to increase along with spurious modes, which would be detrimental for the signal transmission.

The next figures show the cable characterisation, the VNA data of the U waveguide at powers [0, -15, +15] dBm, where $H = 0$ T, as well as the data of the U waveguide (blue) and the commercial GCPW (red) in three different bias fields, $H = [0, 0.1, 0.84]$ T, with the input power set to 0 dBm. All plots were created in Origin.

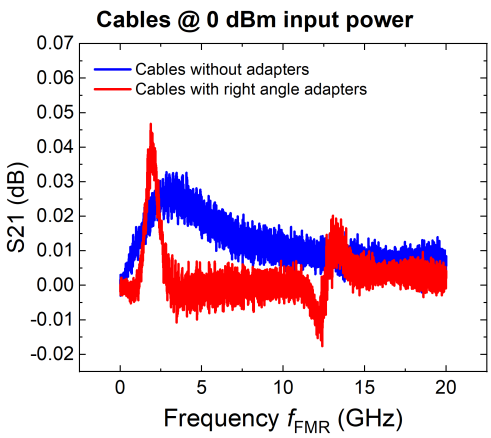

(a) The S21 parameter of the cables without (blue) and with adapters (red).

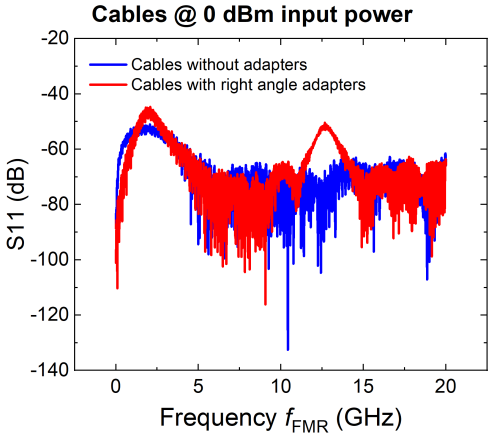

(b) The S11 parameter of the cables without (blue) and with adapters (red).

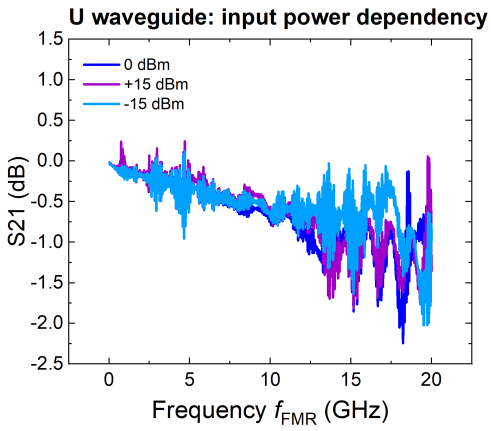

(a) The S21 parameter of the U waveguide at 0 dBm (blue), -15 dBm (azure), and +15 dBm (purple).

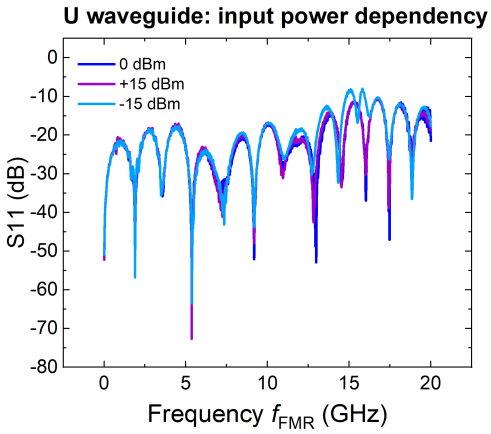

(b) The S11 parameter of the U waveguide at 0 dBm (blue), -15 dBm (azure), and +15 dBm (purple).

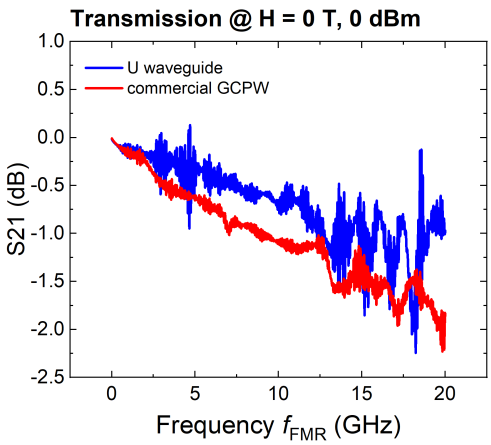

(a) The S21 parameter of the U (blue) and the GCPW (red) at H = 0 T, 0 dBm.

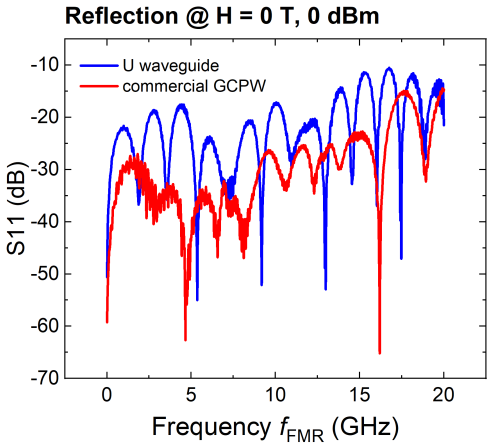

(b) The S11 parameter of the U (blue) and the GCPW (red) at H = 0 T, 0 dBm.

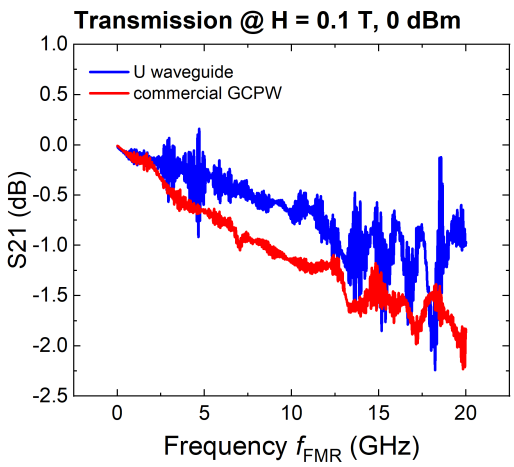

(a) The S21 parameter of the U (blue) and the GCPW (red) at H = 0.1 T, 0 dBm.

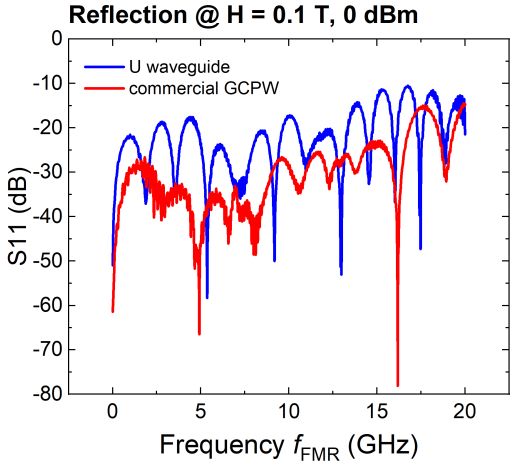

(b) The S11 parameter of the U (blue) and the GCPW (red) at H = 0.1 T, 0 dBm.

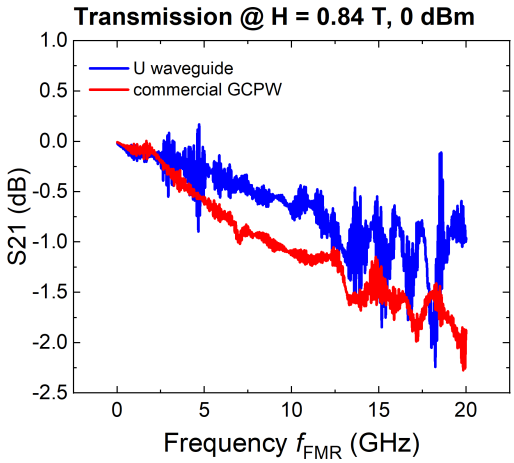

(a) The S21 parameter of the U (blue) and the GCPW (red) at H = 0.84 T, 0 dBm.

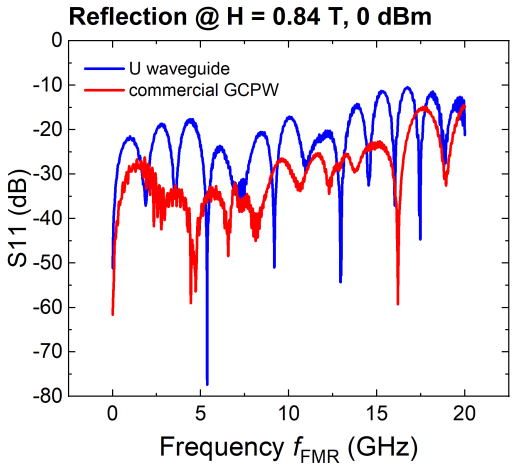

(b) The S21 parameter of the U (blue) and the GCPW (red) at H = 0.84 T, 0 dBm.

The cables have very little effect on the measurements for both waveguides. (S21 maximum fluctuations of 0.035 dB (U) and 0.05 dB (GCPW), S11 below -50 dB (U) and -40 dB (GCPW)) (see fig. 5.5a, 5.5b) On the other hand, the signal in the U waveguide shows better performance at lower input powers. (difference of 0.75 dB between -15 dBm and 0/15 dBm) (see fig. 5.6a) These findings suggest a nonlinear behaviour of the losses versus power. However, this difference could also be attributed to better calibration. The bias field induces no discernible change in the signal. The signal strength is better in the U waveguide than in the GCPW with a difference between 0.5 dB and 1.0 dB. The S21 maximum loss is comparable (-2.5 dB). The signal stability decreases at around 11 GHz (U) and 12.5 GHz (GCPW), which can be seen as oscillations. (see fig. 5.7a, 5.8a, 5.9a) These oscillations are greater for the U waveguide (± 0.6 dB) than for the GCPW (± 0.25 dB). Therefore, the U waveguide retains a stronger, albeit less stable signal in the observed frequency range compared to the commercial GCPW. A GCPW version of the proposed waveguide might be the better option at higher fields/ frequencies.

5.2 Results of the ferromagnetic resonance experiment

Three samples were measured: YIG AZ-E/GGG(111), GaYIG-02B/GGG(111) and GaYIG-05B/GGG(001). The signal power was set to 0 dBm. The graphs in this section include the fits for 105 nm thick GaYIG-02B. The datasets of YIG AZ-E and GaYIG-05B were analysed in a similar fashion, and therefore their graphs have been omitted. The error margins for the results were taken from the fits accordingly. The M_s values cannot be directly determined from the FMR results, thus they have been separately acquired for the Ga:YIG samples through vibrating sample magnetometry (VSM), and will be used in the analysis. For YIG, the M_s value was adopted from [2].

5.2.1 In plane magnetisation of the sample along $[11\bar{2}]$

For a free electron, the gyromagnetic ratio lies at about 176 rad/(ns T), and it can be fixed or fitted for YIG samples. The experimental value of γ has been calculated with the $[11\bar{2}]$ dataset and equation (4.4). (see fig. 5.10) The fit returns $\gamma \approx 179$ rad/(ns T), which comes close to the fixed value. The effective magnetisation is negative, with $\mu_0 M_{eff}$ = -46.5 mT. In pure YIG, the anisotropy contributions are either absorbed into M_s, or combined into one term. [62] This is done because H_c and H_{u1} are two orders of magnitude smaller than M_s. In contrast, in Ga:YIG the anisotropy fields increase, while M_s decreases, thus yielding a negative M_{eff}. This observed trend is partially due to the magnetic compensation in Ga:YIG, where the nonmagnetic Ga^{3+} ions substitute the Fe^{3+} ions in the tetrahedral sublattice, which leads to a lower overall M_s. The other reason is the greater H_{u1} field arising from the higher lattice misfit strain between Ga:YIG and GGG.

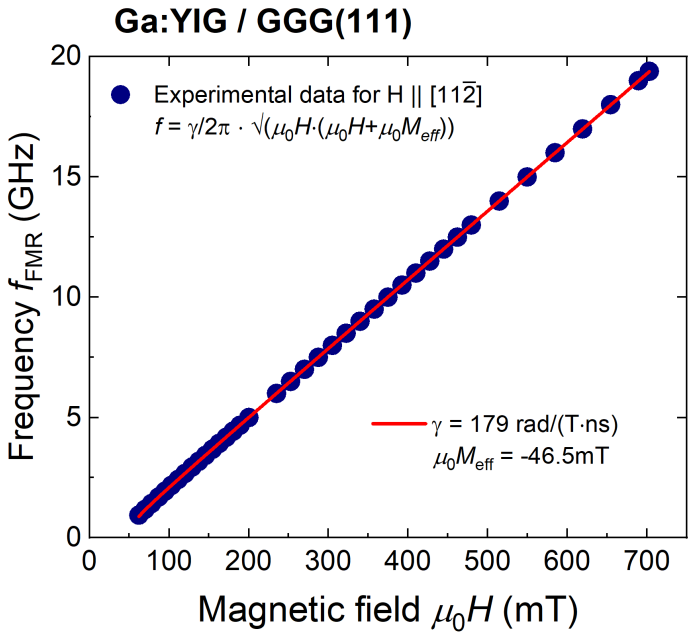

Figure 5.10: The experimental VNA FMR data (blue dots) and the simplified Kittel equation fit (red line) of the 105 nm thick Ga:YIG film grown on GGG(111). The fit returns γ and $\mu_0 M_{eff}$ for the $[11\bar{2}]$ dataset.

5.2.2 In plane magnetisation of the sample along $[1\bar{1}0]$

The cubic anisotropy is obtained by fixing γ and M_{eff}, and fitting the data to equation (4.4). (see fig. 5.11) It was found to be $\mu_0 H_c = -4.2 \pm 0.7$ mT, which is in good agreement with -4.1 mT for 45 nm thick GaYIG reported in [29]. The uniaxial anisotropy of the first order is then given by M_{eff} and H_c, where $\mu_0 H_{u1} = 74.8 \pm 1.0$ mT. Comparably, H_{u1} is one order smaller in pure YIG, implying the presence of a great PMA in Ga:YIG films.

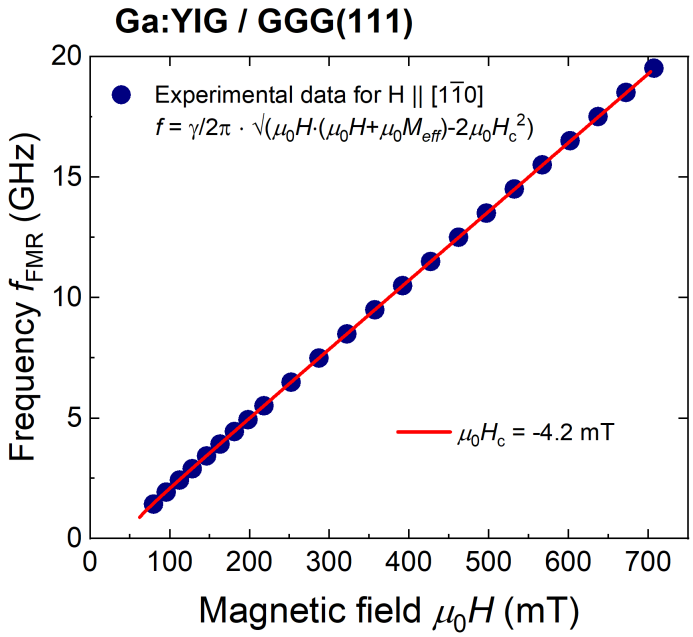

Figure 5.11: The experimental VNA FMR data (blue dots) and the simplified Kittel equation fit (red line) of the 105 nm thick Ga:YIG film grown on GGG(111). The fit returns $\mu_0 H_c$ for the $[1\bar{1}0]$ dataset.

5.2.3 Out of plane magnetisation of the sample

The uniaxial anisotropy of the second order is acquired by the OOP dataset with the equation (4.5), where all the other parameters are constants, so that $\mu_0 H_{u2} = 2.1 \pm 0.1$ mT. (see fig. 5.12)

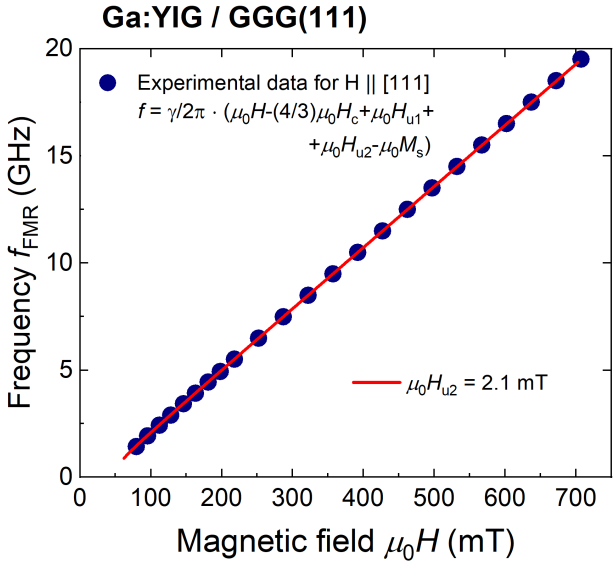

Figure 5.12: The experimental VNA FMR data (blue dots) and the simplified Kittel equation fit (red line) of the 105 nm thick Ga:YIG film grown on GGG(111). The fit returns $\mu_0 H_{u2}$ for the [111] dataset.

5.2.4 Damping parameters

The parameters α_G and $\mu_0 \Delta H(0)$ were determined with the corresponding formula (4.9). (see fig. 5.13) It was found that $\alpha_G = 4.6 \pm 0.28 \cdot 10^{-4}$ ($[11\bar{2}]$), $\alpha_G = 4.9 \pm 0.52 \cdot 10^{-4}$ ($[1\bar{1}0]$). The dissimilar values for α_G along $[11\bar{2}]$ and $[1\bar{1}0]$ could be attributed either to the influence of $\mu_0 \Delta H(0)$, or to the size of the error bars. A more thorough study would be necessary to confirm the origin of this deviation. Several works list their Gilbert damping parameters, including $\alpha_G = 0.4 \cdot 10^{-4}$ for YIG disks [63] and $\alpha_G = 1.25 \cdot 10^{-4} ... 2.44 \cdot 10^{-4}$ for Ga:YIG disks (concentration of Ga atoms $x_{Ga} = 0.78$ ... 0.88) [64] made from bulk crystal, as well as $\alpha_G = 0.4 \cdot 10^{-4}$ (t = 23 µm) [64] and $\alpha_G = 0.5 \pm 0.52 \cdot 10^{-4}$ (t = 3 µm) [65] for epitaxially grown µm thick YIG. Furthmore, the sub-100 nm thick high quality LPE YIG films are reported to have $\alpha_G = 1.0 \cdot 10^{-4} ... 1.2 \cdot 10^{-4}$ (t = 42...11 nm) [21]. In addition, Carmiggelt et al. calculated $\alpha_G = 1.0 \cdot 10^{-3}$ for a 45 nm thick Ga:YIG film. [29] The 45 nm thick sample has a lower M_s, therefore the larger damping is in good agreement with the damping present in the 105 nm thick sample analysed in this thesis. The relaxation parameters are significantly better compared to the other studied YIG-substituted materials, e.g. Mn:YIG [25], Bi:YIG [26]. Soumah et al. reported an exceptionally low $\alpha_G = 3.0 \cdot 10^{-4}$ and $\mu_0 \Delta H = 0.4$ mT in their Bi:YIG film, but these only apply to a measurement setup, where the polar angle θ is varied between 27° and 34° to minimise the linewidth at each frequency. For $\theta = 0°$, $\mu_0 \Delta H(0) \approx 31$ mT, which is two orders of magnitude greater compared to the investigated samples.

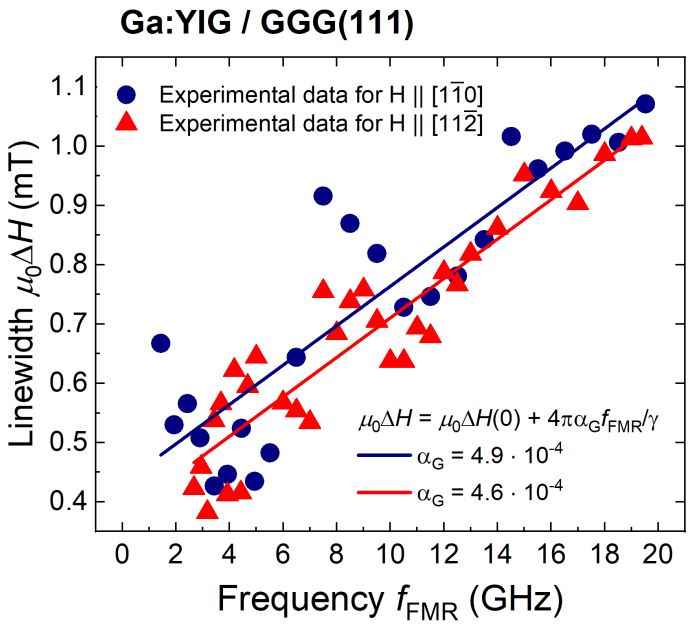

Figure 5.13: The linewidth $\mu_0\Delta H$ recalculated with the experimentally measured linewidth Δf for **H** || [1$\bar{1}$0] (blue dots), **H** || [11$\bar{2}$] (red triangles) and the linewidth equation fits (blue and red line, respectively) of the 105 nm thick Ga:YIG film grown on GGG(111). The fits return α_G and $\mu_0\Delta H(0)$ for the IP datasets.

An overview of the magnetic parameters is given in the tables 5.1 and 5.2.

Sample	thickness	$\mu_0 M_s$ [mT]	$\mu_0 H_c$ [mT]	$\mu_0 H_{u1}$ [mT]	$\mu_0 H_{u2}$ [mT]
YIG AZ-E	97 nm	182.4 ± 1.8	-5.1 ± 0.5	-3.5 ± 0.5	3.6 ± 0.5
GaYIG-02B	105 nm	24.4 (VSM)	-4.2 ± 0.7	74.8 ± 1.0	2.1 ± 0.1
GaYIG-05B	96 nm	21.7 (VSM)	-5.3 ± 0.6	92.4 ± 1.7	5.2 ± 0.2

Table 5.1: The results for $\mu_0 M_s$ and all anisotropy fields.

Sample	γ [rad/(ns T)]	$\alpha_G[10^{-4}]$		$\mu_0\Delta H(0)$ [mT]	
		[11$\bar{2}$]	[1$\bar{1}$0]	[11$\bar{2}$]	[1$\bar{1}$0]
YIG AZ-E	177	1.3 ± 0.15	0.6 ± 0.16	0.1 ± 0.01	0.2 ± 0.01
GaYIG-02B	179	4.6 ± 0.28	4.9 ± 0.52	0.4 ± 0.02	0.4 ± 0.04
		[100]	[1$\bar{1}$0]	[100]	[1$\bar{1}$0]
GaYIG-05B	179	8.4 ± 0.85	6.7 ± 0.68	0.4 ± 0.06	0.4 ± 0.05

Table 5.2: The results for γ, α_G and $\mu_0\Delta H(0)$.

6 Conclusion and outlook

The proposed U waveguide allows bigger, more homogeneous fields and a stronger signal compared to the commercial GCPW. This is due to the absence of right-angle adapters and the subsequent tighter magnet pole spacing. However, there are oscillations visible in the signal, which suggest the presence of radiation losses. To alleviate this issue, the waveguide design could be revisited to change it into a GCPW, and optimise the performance also at higher frequencies.

For all analysed samples, γ, H_c and H_{u2} remain roughly the same. The value γ for a free electron lies at around 176 rad/(ns T), which is in good agreement with the fits. H_{u1}, on the other hand, changes its sign for the Ga:YIG samples and increases by a factor of about 21 and 24, for GaYIG-02B and GaYIG-05B, respectively. This implies a strong uniaxial strain, resulting in a pronounced PMA. The acquired M_s are lower by a factor of approx. 8 compared to the YIG sample, while α_G is 11 times greater along $[1\bar{1}0]$ in GaYIG-05B. The increase in α_G counteracts the higher group velocity of the SWs. Nevertheless, the SWs are predominantly of isotropic nature and faster than in pure YIG. Compared to other YIG-substituted materials [23] [24] [25] [26] [27], the parameters α_G and $\mu_0\Delta H(0)$ are among the lowest values reported so far.

To summarise, Ga:YIG removes the need for high external fields due to its PMA, and it enables fast, isotropic SW transport. These findings suggest that Ga:YIG is a highly competitive material in the field of magnonics.

Bibliography

[1] V. B. Bobkov and I. V. Zavislyak, "Equilibrium State and Magnetic Permeability Tensor of the Epitaxial Ferrite Films," *phys. stat. sol (a)*, vol. 164, no. 2, pp. 791–804, 1997.

[2] T. Böttcher et al., "Fast long-wavelength exchange spin waves in partially compensated ga:yig," *Applied Physics Letters*, vol. 120, no. 10, p. 102401, 2022.

[3] K. M. Krishnan, *Fundamentals and Applications of Magnetic Materials*, ch. 3.8. Oxford University Press, 2016.

[4] T. C. Edwards and M. B. Steer, *Microstrip at High Frequencies*, ch. 7, pp. 157–199. John Wiley and Sons, Ltd, 2016.

[5] D. McMahill, "Microstrip analysis/synthesis calculator." `https://wcalc.sourceforge.net/cgi-bin/microstrip.cgi`. accessed: 05.04.2023.

[6] T. C. Edwards and M. B. Steer, *CPW Design Fundamentals*, ch. 14, pp. 384–442. John Wiley and Sons, Ltd, 2016.

[7] H. Jin and R. Vahldieck, "Full-wave analysis of coplanar waveguide discontinuities using the frequency domain tlm method," *IEEE Transactions on Microwave Theory and Techniques*, vol. 41, no. 9, pp. 1538–1542, 1993.

[8] W. Frei, "Using perfectly matched layers and scattering boundary conditions for wave electromagnetics problems." `https://www.comsol.com/blogs/using-perfectly-matched-layers-and-scattering-boundary-conditions-for-wave-electromagnetics-problems`. accessed: 05.04.2023.

[9] A. A. Serga, A. V. Chumak, and B. Hillebrands, "Yig magnonics," *Journal of Physics D: Applied Physics*, vol. 43, p. 264002, jun 2010.

[10] F. Bloch, "Zur theorie des ferromagnetismus," *Zeitschrift für Physik*, vol. 61, pp. 206–219, 1930.

[11] A. Gurevich and G. Melkov, *Magnetization Oscillations and Waves*. CRC Press, 1996.

[12] D. D. Stancil and A. Prabhakar, *Spin Waves*. Springer, 2009.

[13] B. Kalinikos, N. Kovshikov, P. Kolodin, and A. Slavin, "Observation of dipole-exchange spin wave solitons in tangentially magnetised ferromagnetic films," *Solid State Communications*, vol. 74, no. 9, pp. 989–993, 1990.

[14] A. Serga, S. Demokritov, B. Hillebrands, and A. Slavin, "Self-generation of two-dimensional spin-wave bullets," *Physical review letters*, vol. 92, p. 117203, 04 2004.

[15] G. A. Melkov, A. A. Serga, V. S. Tiberkevich, A. N. Oliynyk, and A. N. Slavin, "Wave front reversal of a dipolar spin wave pulse in a nonstationary three-wave parametric interaction," *Phys. Rev. Lett.*, vol. 84, pp. 3438–3441, Apr 2000.

[16] A. A. Serga et al., "Parametric generation of forward and phase-conjugated spin-wave bullets in magnetic films," *Phys. Rev. Lett.*, vol. 94, p. 167202, Apr 2005.

[17] A. Serga et al., "Bose-einstein condensation in an ultra-hot gas of pumped magnons," *Nature communications*, vol. 5, p. 3452, 03 2014.

[18] D. Bozhko et al., "Supercurrent in a room-temperature bose–einstein magnon condensate," *Nature Physics*, vol. 12, 08 2016.

[19] A. Barman et al., "The 2021 magnonics roadmap," *Journal of Physics: Condensed Matter*, vol. 33, p. 413001, aug 2021.

[20] A. Chumak et al., "Advances in magnetics roadmap on spin-wave computing," *IEEE Transactions on Magnetics*, vol. 58, no. 6, pp. 1–72, 2022.

[21] C. Dubs et al., "Low damping and microstructural perfection of sub-40nm-thin yttrium iron garnet films grown by liquid phase epitaxy," *Phys. Rev. Mater.*, vol. 4, p. 024416, Feb 2020.

[22] B. Heinz et al., "Long-range spin-wave propagation in transversely magnetized nanoscaled conduits," *Applied Physics Letters*, vol. 118, no. 13, p. 132406, 2021.

[23] L. Soumah et al., "Ultra-low damping insulating magnetic thin films get perpendicular," *Nature Communications*, vol. 9, 08 2018.

[24] C. N. Wu et al., "High-quality single-crystal thulium iron garnet films with perpendicular magnetic anisotropy by off-axis sputtering," *AIP Advances*, vol. 8, no. 5, p. 055904, 2018.

[25] J. Chen et al., "Spin wave propagation in ultrathin magnetic insulators with perpendicular magnetic anisotropy," *Applied Physics Letters*, vol. 114, no. 21, p. 212401, 2019.

[26] Y. Lin et al., "Bi-yig ferrimagnetic insulator nanometer films with large perpendicular magnetic anisotropy and narrow ferromagnetic resonance linewidth," *Journal of Magnetism and Magnetic Materials*, vol. 496, p. 165886, 2020.

[27] Q.-H. Yang et al., "The absorption property of single crystal lubiig garnet film in terahertz band," *Journal of Applied Physics*, vol. 111, no. 7, p. 07A513, 2012.

[28] P. Görnert and C. G. D'ambly, "Investigations of the growth and the saturation magnetization of garnet single crystals y3fe5xgaxo12 and y3fe5xalxo12," *physica status solidi (a)*, vol. 29, no. 1, pp. 95–105, 1975.

[29] J. J. Carmiggelt et al., "Electrical spectroscopy of the spin-wave dispersion and bistability in gallium-doped yttrium iron garnet," *Applied Physics Letters*, vol. 119, no. 20, p. 202403, 2021.

[30] K. M. Krishnan, *Fundamentals and Applications of Magnetic Materials*. Oxford University Press, 2016.

[31] K. M. Krishnan, *Fundamentals and Applications of Magnetic Materials*, ch. 1.2. Oxford University Press, 2016.

[32] K. M. Krishnan, *Fundamentals and Applications of Magnetic Materials*, ch. 2.5. Oxford University Press, 2016.

[33] G. Gabrielse and D. Hanneke, "Precision pins down the electron's magnetism." `https://web.archive.org/web/20061018223513/http://www.cerncourier.com/main/article/46/8/20`. accessed: 02.04.2023.

[34] K. M. Krishnan, *Fundamentals and Applications of Magnetic Materials*, ch. 1.4. Oxford University Press, 2016.

[35] K. M. Krishnan, *Fundamentals and Applications of Magnetic Materials*, ch. 3.5. Oxford University Press, 2016.

[36] A. Gurevich and G. Melkov, *Magnetization Oscillations and Waves*, ch. 1.5. CRC Press, 1996.

[37] K. M. Krishnan, *Fundamentals and Applications of Magnetic Materials*, ch. 1.11. Oxford University Press, 2016.

[38] A. Gurevich and G. Melkov, *Magnetization Oscillations and Waves*, ch. 2.1. CRC Press, 1996.

[39] A. Gurevich and G. Melkov, *Magnetization Oscillations and Waves*, ch. 1.3. CRC Press, 1996.

[40] H. Szymczak and N. Tsuya, "Phenomenological Theory of Magnetostriction and Growth-Induced Anisotropy in Garnet Films," *physica status solidi (a)*, vol. 54, no. 1, pp. 117–120, 1979.

[41] C. Kittel, "Ferromagnetic Resonance," *J. Phys. Radium*, vol. 12, no. 3, pp. 291–302, 1951.

[42] L. Baselgia et al., "Derivation of the resonance frequency from the free energy of ferromagnets," *Physical Review B*, vol. 38, no. 4, pp. 2237–2242, 1988.

[43] S. S. Kalarickal et al., "Ferromagnetic resonance linewidth in metallic thin films: Comparison of measurement methods," *J. Appl. Phys*, vol. 99, no. 9, p. 093909, 2006.

[44] I. S. Maksymov and M. Kostylev, "Broadband stripline ferromagnetic resonance spectroscopy of ferromagnetic films, multilayers and nanostructures," *Physica E: Low-dimensional Systems and Nanostructures*, vol. 69, pp. 253–293, 2015.

[45] T. C. Edwards and M. B. Steer, *Microwave Network Analysis*, ch. 3, pp. 51–75. John Wiley and Sons, Ltd, 2016.

[46] T. C. Edwards and M. B. Steer, *Fundamentals of Signal Transmission on Interconnects*, ch. 2, pp. 19–50. John Wiley and Sons, Ltd, 2016.

[47] G. Vendelin, "Limitations on stripline Q," *Microwave Journal*, pp. 63–69, 1970.

[48] T. C. Edwards and M. B. Steer, *Planar Interconnect Technologies*, ch. 5, pp. 89–119. John Wiley and Sons, Ltd, 2016.

[49] T. C. Edwards and M. B. Steer, *Microstrip Design at Low Frequencies*, ch. 6, pp. 120–156. John Wiley and Sons, Ltd, 2016.

[50] E. Hammerstad and O. Jensen, "Accurate models for microstrip computer-aided design," in *1980 IEEE MTT-S International Microwave symposium Digest*, pp. 407–409, 1980.

[51] T. C. Edwards and M. B. Steer, *Loss and Power-dependent Effects in Microstrip*, ch. 8, pp. 200–226. John Wiley and Sons, Ltd, 2016.

[52] T. C. Edwards and M. B. Steer, *Discontinuities in Microstrip*, ch. 9, pp. 227–267. John Wiley and Sons, Ltd, 2016.

[53] T. C. Edwards and M. B. Steer, *Transitions*, ch. 17, pp. 488–513. John Wiley and Sons, Ltd, 2016.

[54] A. Sain and K. L. Melde, "Impact of ground via placement in grounded coplanar waveguide interconnects," *IEEE Transactions on Components, Packaging and Manufacturing Technology*, vol. 6, no. 1, pp. 136–144, 2016.

[55] R. Quhe et al., "Sub-10 nm two-dimensional transistors: Theory and experiment," *Physics Reports*, vol. 938, pp. 1–72, 2021. Sub-10 nm two-dimensional transistors: Theory and experiment.

[56] T. Iizuka, *CMOS technology scaling and its implications*, p. 1–20. Cambridge University Press, 2015.

[57] D.J. Frank et al., "Device scaling limits of si mosfets and their application dependencies," *Proceedings of the IEEE*, vol. 89, no. 3, pp. 259–288, 2001.

[58] A. V. Chumak, *Magnon Spintronics*, ch. 6. CRC Press, 2019.

[59] B. Heinz et al., "Propagation of spin-wave packets in individual nanosized yttrium iron garnet magnonic conduits," *Nano Letters*, vol. 20, no. 6, pp. 4220–4227, 2020. PMID: 32329620.

[60] C. E. Patton, "Linewidth and relaxation processes for the main resonance in the spin-wave spectra of ni–fe alloy films," *Journal of Applied Physics*, vol. 39, no. 7, pp. 3060–3068, 1968.

[61] P. Pirro et al., "Spin-wave excitation and propagation in microstructured waveguides of yttrium iron garnet/pt bilayers," *Applied Physics Letters*, vol. 104, no. 1, p. 012402, 2014.

[62] M. Onbasli et al., "Pulsed laser deposition of epitaxial yttrium iron garnet films with low gilbert damping and bulk-like magnetization," *Appl. Phys. Lett. Mater.*, vol. 2, p. 106102, 10 2014.

[63] P. Roschmann, "Annealing effects on fmr linewidth in ga substituted yig," *IEEE Transactions on Magnetics*, vol. 17, no. 6, pp. 2973–2975, 1981.

[64] P. Roschmann and W. Tolksdorf, "Epitaxial growth and annealing control of fmr properties of thick homogeneous ga substituted yttrium iron garnet films," *Materials Research Bulletin*, vol. 18, no. 4, pp. 449–459, 1983.

[65] C. Dubs et al., "Sub-micrometer yttrium iron garnet lpe films with low ferromagnetic resonance losses," *Journal of Physics D: Applied Physics*, vol. 50, p. 204005, apr 2017.

Acronyms

AC Alternating Current. 16

BVMSW Backward Volume Magnetostatic Spin Wave. 32

CPW Coplanar Waveguide. 26

DC Direct Current. 21

EM Electromagnetic. 15

FG-GCPW Finite Ground Grounded Coplanar Waveguide. xi, 27

FMR Ferromagnetic Resonance. 14

FVMSW Forward Volume Magnetostatic Spin Wave. 32

FWHM Full Width At Half Maximum. 36

Ga:YIG Gallium Doped Yttrium Iron Garnet. 1

GCPW Grounded Coplanar Waveguide. xi, 27

GGG Gadolinium Gallium Garnet. 33

IP In Plane. 32

LLG Landau Lifshitz Gilbert (equation). 12

LPE Liquid Phase Epitaxy. 33

MCA Magnetocrystalline Anisotropy. 13

MSSW Magnetostatic Surface Spin Wave. 32

OOP Out Of Plane. 32

PEC Perfect Electric Conductor. 28

PMA Perpendicular Magnetic Anisotropy. 32

PML Perfectly Matched Layers. 28

QTEM Quasi Transverse Electromagnetic. 22

RF Radio Frequency. 21

SBC Scattering Boundary Condition. 28

SW Spin Wave. 31

TE Transverse Electric. 23

TEM Transverse Electromagnetic. 22

TM Transverse Magnetic. 23

VNA Vector Network Analyzer. 16

VSM Vibrating Sample Magnetometry. 42

VSWR Voltage Standing Wave Ratio. 20

YIG Yttrium Iron Garnet. 1